30 kW Bidirectional Inductive Power Transfer Charger With Intermediate Coil for EV Applications

Nikola Mirković, *Student Member, IEEE*, Luis Ruiz Chamorro, Alberto Delgado, *Member, IEEE*, Pedro Alou, *Member, IEEE*, and Miroslav Vasić, *Senior Member, IEEE*

***Abstract*—High power, highly efficient, and robust bidirectional inductive power transfer (IPT) system based on three windings, used for automotive applications is considered in this article. Compensation strategies are revised, and benefits of three-coil system are outlined. A simple equivalent circuit model of the three-coil system is derived in order to improve the comprehension of the system. Tuning methodology for the compensation circuit of the three-coil IPT system, suitable for the considered application is proposed, together with the guidelines for its implementation. All of the coils were designed and optimized together with the proposed compensation circuitry, with the employed resonant dual active bridge (DAB) topology. IPT prototype for 30 kW has been realized according to the design proposal, and tested, transferring power levels between and 37.4 kW, with the varying air gap between and 150 mm, with the overall system efficiency ranging from 91.29% up to 96.72%. Behavior and efficiency of the system were tested using constant-power, constant-current, and constant-voltage charging methods, and both in grid-to-vehicle and vehicle-to-grid modes of operation.**

***Index Terms*—Compensation, inductive power transfer (IPT), three-coil system.**

I. Introduction

In RECENT years, wireless chargers based on inductive power transfer (IPT) actively gain popularity in the area of electric vehicles (EVs) [1], [2], [3]. They present an attractive alternative to the conventional cable chargers due to handling simplicity that they offer to the end-user. From the aspect of a local microgrid, a way to enhance an EV battery charger is by giving it a bidirectionality feature. By doing so, the car battery is turned into an energy bank, capable of both taking and providing power when needed.

The core of every IPT system is the coupled coils, via whom, the energy is being exchanged between the two parts of the system. Due to the lack of magnetic core, coupling coefficient between the coils is low, ranging between 8% and 25% [4]. To overcome the problem of low coupling between the coils, various compensation topologies are presented in state-of-the-art as possible solutions to this problem [5].

Due to its simplicity the most common one is the series–series (S–S) compensation strategy [6], [7], [8], [9], [10], [11]. Besides this one, three more basic compensation strategies can be singled out from the group of fundamental ones, and those are: series–parallel (S–P), parallel–series (P-S), and parallel-parallel (P–P) [12]. From the group of more complex ones, the application of double-sided LCC compensation strategy [13] is present throughout the literature [14], [15], [16], [17]. By introducing more reactive elements to the system, higher efficiency of the system is achieved, even in the conditions of misalignment [13], all at the cost of reduced simplicity of the system. Also, it is possible to find compensation strategies that are a combination of some of the basic ones such as series, on one side of the system, and a complex LCC on the other side, i.e., the LCC–S compensation strategy [18], [19], [20].

Alongside with the research tied to the previously mentioned compensation strategies that are intended for two-coil systems, IPT systems with three [21], [22], [23], [24], [25], [26], [27], [28], [29], [30], [31], [32], [33], [34], [35] and four [36], [37], [38], [39], [40], [41] coils were analyzed. According to [42], four-coil systems are more suitable for high efficiency, low power applications, as they offer higher power transfer efficiency but lower power delivered to the load comparing to the three-coil systems. While offering slightly reduced efficiency comparing to the four-coil systems, three-coil systems prove themselves more suitable for applications requiring high power transfer capability, i.e., they present a potential candidate for electric vehicle (EV) charging applications. Furthermore, Nguyen et al. [43] compared efficiencies of the SS compensated system, LCC–S compensated system and the three-coil system, showing that the last two have similar efficiencies, both significantly larger than the efficiency of the first one. Also, Yang et al. [44] and Mirkovic et al. [45] showed the possibility of increased power transfer capability of the three-coil system under misalignment conditions. All of the previously stated articles provide a reasonable argument for continuing research of the three-coil systems in EV charging applications.

In the current state-of-the-art there is a significant number of works investigating the three-coil IPT systems. Zhong et al. [21], Zhang et al. [27], and Liu et al. [31] analyzed and compared two-coil and three-coil systems, proving that it is possible to make a three-coil IPT system more efficient than a two-coil one, as well as that the three-coil IPT system exhibits higher

Manuscript received 5 December 2023; revised 2 February 2024 and 15 March 2024; accepted 11 April 2024. Date of publication 16 April 2024; date of current version 16 May 2024. This work was supported by project PID2020-117582RB-I00 funded by MCIN/AEI/10.13039/501100011033. Recommended for publication by Associate Editor D. Qiu. *(Corresponding author: Nikola Mirković.)*

The authors are with the Centro de Electrónica Industrial, Universidad Politécnica de Madrid, 28006 Madrid, Spain (e-mail: n.mirkovic@upm.es).

Color versions of one or more figures in this article are available at https://doi.org/10.1109/TPEL.2024.3389129.

Digital Object Identifier 10.1109/TPEL.2024.3389129

efficiency stiffness against load variations and reduced EMF emissions. Being that the most common way of charging the contemporary Li-ion batteries is the constant-current/constant-voltage (CC/CV) charging, a lot of the works related with the three-coil IPT systems [24], [26], [28], [29], [30] propose a certain hybrid topology or control technique that would allow the CC/CV charging of the EV battery. The IPT system with an additional diode rectifier added to the assistive coil circuit is given in [24], allowing for the seamless change between CC and CV modes of operation. In [26], authors proposed a hybrid topology, adding two four-quadrant switches and several passive elements in order to achieve different resonance behaviors of the system in dependence on the CC or CV charging mode of operation. Similar approach to this one is seen in [29]. Somewhat simpler solution is present in [28], comprising a reconfigurable topology that can change between the two-coil and three-coil topologies, depending whether CC or CV mode of operation is required. Another example of a reconfigurable topology is present in [46], where authors proposed a system that can change between two-coil, three-coil and four-coil topology, and in that way preserve the system efficiency at high level over a large span of varying distances between transmitter and receiver. On the other side, Yang et al. [30] applied a frequency control to the three-coil S–S–P compensated system in order to change between different charging modes. Frequency control of a three-coil IPT is as well present in [25], where Moon et al. proposed an optimal design method of the three-coil IPT system using the second resonance frequency with the bifurcation phenomenon. A novel S–S–LCLCC compensation method for three-coil IPT is proposed in [22], showing improved misalignment and efficiency stiffness of the IPT system. Lee et al. [33] investigated a three-coil IPT system with triangular shape transmitter coils for achieving better misalignment tolerance. Bilal et al. [34] analyzed the optimal placement of the intermediate coil for transferring power across large air gaps. A very interesting approach when it comes to the three-coil IPT systems can be seen in [23], where Wang et al. proposed a special design of the magnetic coupler to avoid unwanted coupling between certain windings, and using the S–S–S compensation strategy achieve load-independent CV charging characteristics. When it comes to the matter of bidirectionality, all of the previously mentioned works are unidirectional. Complexity of some of them is relatively high as they incorporate additional four-quadrant switches and several passives in order to achieve CC/CV charging operation. On the other hand, others rely on varying the operating frequency, making those solutions challenging for implementation in the EV charging applications as the current standard proposal predicts very narrow window of operable frequencies of the system, ranging between and 90 kHz [4]. From the point of view of the charging method, there are other charging methods mentioned in the literature, such as constant-power/constant-voltage (CP/CV) [18], [48], [49] or pulsed-current charging methods [50], [51]. While the latter one is still being investigated the first one has known advantages over the CC/CV charging method such as longer battery lifecycle and utilizing maximum power transfer capacity of the charger.

Motivated by the high efficiency of three-coil systems that are present in the state-of-the-art, and by the lack of bidirectional solutions, in this article, we propose a tuning method and a design procedure for the S–S–S compensated three-coil bidirectional IPT system intended for the EV charging applications that is given in Fig. 1. The considered system may contain added serial inductors on the primary and/or secondary side, as it will be explained in the following Sections. Third coil is added in order to reduce the entire system to the equivalent inductor seen between the primary and secondary sides and to provide the required reactive power for the system operation, thus lowering the current stress on the semiconductor devices and increasing the overall efficiency of the charger. Number of added compensation elements in the system is lower comparing to the most of the previously mentioned articles, thus achieving high simplicity and low volume of the system. Capacitors of the system are tuned in a manner to suit the application of high-power, bidirectional EV charger. The compensation method and the basic functionality of the proposed magnetic link are briefly explained in our previous work [52]. This article is completely dedicated to the compensation and design of the magnetic link of the discussed three-coil bidirectional IPT system with its main contributions being, in the order that they appear in the article.

1) The equivalent circuit of the three-coil system is derived and used for all the analysis that were considered, significantly improving the system comprehension comparing to the understanding provided by the mathematical model.
2) The tuning method for the capacitors of the S–S–S compensated three-coil bidirectional IPT charger for the EVs, that allows seamless implementation of any of the previously mentioned charging methods (CC/CV, CP/CV) while being suited for the bidirectional energy transfer, allowing for seamless transitions between grid-to-vehicle (G2V) and vehicle-to-grid (V2G) modes of operation. Charging method of the charger proposed in this work is not tied with the topology itself, rather it depends on the control that is implemented on the vehicle side of the system and on the battery management system (BMS).
3) The design procedure of the magnetic link for the proposed tuning method that emphasizes the high efficiency of the system and minimizes the weight that is being added to the vehicle.

The rest of the article is organized as follows. In Section II equivalent circuit model of the three-coil system is derived. Section III explains the functionality of the proposed IPT charger. Design procedure of the system is outlined in Section IV. Experimental results are given in Section V. Finally, Section VI concludes this article

II. Model of the Three-Coil IPT System

In order to facilitate the understanding of the three-coil IPT system that is given in Fig. 1, an equivalent circuit will be used and parameters connecting the real parameters of the system with the parameters of the equivalent circuit will be derived. The three coupled inductors are given in Fig. 2(a). Schematic of the equivalent circuit based on a three-winding transformer is given in Fig. 2(b). Equations based on Kirchhoff's laws for the

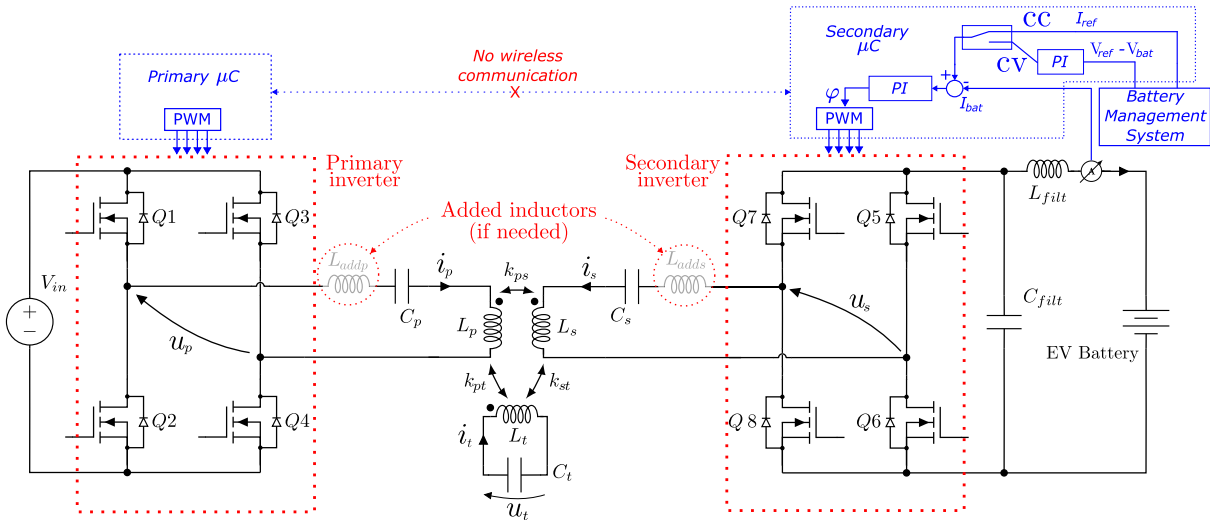

Fig. 1. Considered three-coil bidirectional IPT system.

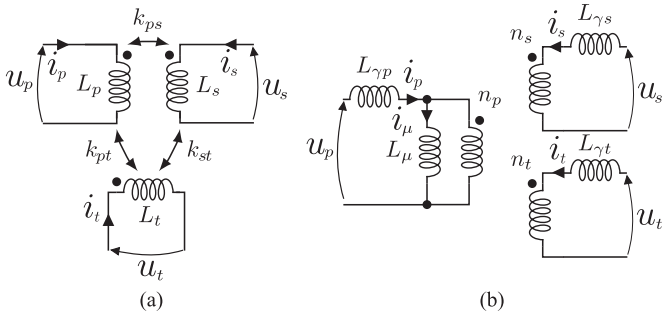

Fig. 2. (a) Three coupled inductors. (b) Equivalent circuit of the three coupled inductors based on a three-winding transformer.

three coupled inductors are the following:

$$u_p = L_p \frac{\mathrm{d}i_p}{\mathrm{d}t} + L_{ps} \frac{\mathrm{d}i_s}{\mathrm{d}t} + L_{pt} \frac{\mathrm{d}i_t}{\mathrm{d}t} \tag{1}$$

$$u_s = L_{ps} \frac{\mathrm{d}i_p}{\mathrm{d}t} + L_s \frac{\mathrm{d}i_s}{\mathrm{d}t} + L_{st} \frac{\mathrm{d}i_t}{\mathrm{d}t} \tag{2}$$

$$u_t = L_{pt} \frac{\mathrm{d}i_p}{\mathrm{d}t} + L_{st} \frac{\mathrm{d}i_s}{\mathrm{d}t} + L_t \frac{\mathrm{d}i_t}{\mathrm{d}t} \tag{3}$$

where $L_{ps} = k_{ps}\sqrt{L_p L_s}$, $L_{pt} = k_{pt}\sqrt{L_p L_t}$, and $L_{st} = k_{st}\sqrt{L_s L_t}$. Analogous to this, equations based on Kirchhoff's laws can be written for the given equivalent circuit

$$u_p = (L_{\gamma p} + L_\mu) \frac{\mathrm{d}i_p}{\mathrm{d}t} + L_\mu \frac{n_s}{n_p} \frac{\mathrm{d}i_s}{\mathrm{d}t} + L_\mu \frac{n_t}{n_p} \frac{\mathrm{d}i_t}{\mathrm{d}t} \tag{4}$$

$$u_s = L_\mu \frac{n_s}{n_p} \frac{\mathrm{d}i_p}{\mathrm{d}t} + \left(L_\mu \frac{n_s^2}{n_p^2} + L_{\gamma s} \right) \frac{\mathrm{d}i_s}{\mathrm{d}t} + L_\mu \frac{n_s n_t}{n_p^2} \frac{\mathrm{d}i_t}{\mathrm{d}t} \tag{5}$$

$$u_t = L_\mu \frac{n_t}{n_p} \frac{\mathrm{d}i_p}{\mathrm{d}t} + L_\mu \frac{n_s n_t}{n_p^2} \frac{\mathrm{d}i_s}{\mathrm{d}t} + \left(L_\mu \frac{n_t^2}{n_p^2} + L_{\gamma t} \right) \frac{\mathrm{d}i_t}{\mathrm{d}t}. \tag{6}$$

The proposed equivalent circuit does not represents a physical equivalent for the considered system, rather a mathematical one, and it should be regarded as such.

Based on the previous systems of (1)–(3) and (4)–(6), it is possible, by equalizing corresponding parts, to express the parameters of the equivalent circuit in dependence on the real parameters of the three coupled inductors. By doing so, one obtains

$$\frac{n_p}{n_s} = \frac{L_{pt}}{L_{st}} \tag{7}$$

$$\frac{n_p}{n_t} = \frac{L_{ps}}{L_{st}} \tag{8}$$

$$L_\mu = \frac{L_{ps} L_{pt}}{L_{st}} \tag{9}$$

$$L_{\gamma p} = L_p - L_\mu \tag{10}$$

$$L_{\gamma s} = L_s - \left(\frac{L_{st}}{L_{pt}} \right)^2 L_\mu \tag{11}$$

$$L_{\gamma t} = L_t - \left(\frac{L_{st}}{L_{ps}} \right)^2 L_\mu. \tag{12}$$

Fig. 3(a) depicts the previously derived equivalent circuit of the three-coil system with compensation applied, with all of the parameters taken to the primary side. The desired outcome of the compensation is given in Fig. 3(b). The basic idea is to reduce the three-coil IPT system to the tightly coupled two-coil system, having an equivalent inductor seen between the primary and secondary sides, where power transfer is controlled like in the case of DAB topology [53], thus achieving good controllability. This is valid for the fundamental frequency, i.e., the operating frequency of the converters. For the harmonic frequencies that are multiples of the fundamental frequency behavior of this system is different from the one of the DAB topology due to its resonant nature. The way of achieving the equality of the S–S–S compensated three-coil system and DAB at fundamental frequency is given in Fig. 3(c). Tertiary capacitor is tuned to resonate with the self-inductance of the tertiary winding, thus compensating for the magnetizing inductance and reducing the current stress on the inverters, allowing for high efficiency of

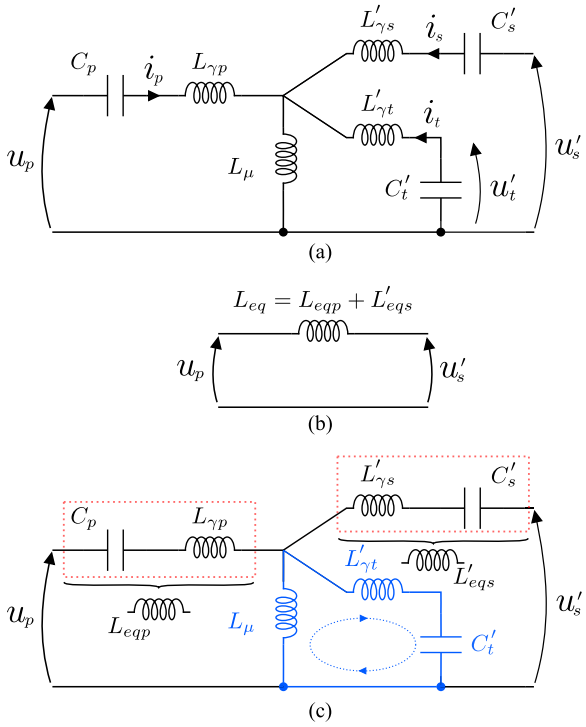

Fig. 3. (a) Compensated equivalent circuit of the three-coil inductor. (b) Desired equivalent circuit. (c) Operating principle of the proposed compensation strategy.

the system, while primary and secondary capacitors are tuned to partially compensate for the primary and secondary leakage inductances, thus leaving a part of them uncompensated, and the equivalent inductance is seen between the primary and secondary sides. Determining the value of the equivalent inductance that is left uncompensated will be discussed in Section IV as this is the matter of the each IPT system in particular and depends on the voltage levels, desired power transfer capability, etc. The following equations define the values of the primary, secondary, and tertiary capacitors, respectively:

$$C_p = \frac{1}{(2\pi f)^2(L_{\gamma p} - L_{\text{eqp}})} \tag{13}$$

$$C_s = \frac{1}{(2\pi f)^2(L_{\gamma s} - L_{\text{eqs}})} \tag{14}$$

$$C_t = \frac{1}{(2\pi f)^2 L_t}. \tag{15}$$

Basic idea of the proposed compensation strategy is stated in this section. In Section IV, where the design of the system is considered, it will be shown that from the point of view of the system efficiency, it can be beneficial to take the tertiary capacitor out from the resonance. In the same section, a guideline for determining L_{eqp} and L_{eqs} will be given. Also, external inductors can be added in series with the primary and/or secondary coils if it contributes the efficiency. However, the main principle given in this section states, the three-coil system is reduced to an equivalent inductor, that is seen between the primary and secondary side.

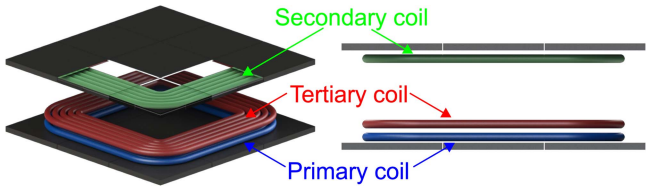

Fig. 4. 3-D model of the proposed three-coil IPT system.

III. Topology and Functionality of the Proposed System

A. Basic Operation Principle

The system topology considered in this work is given in Fig. 1, while the Fig. 4 shows the 3-D model of the coils and their distribution in space. From the converter point of view, there are two inverters, one on the primary side and one on the secondary side. Being that the equivalent circuit of the considered three-coil IPT system is equal to the one given in Fig. 3(b), accounting the first harmonic approximation, the active power that is going from the primary to the secondary side is equal to

$$P = \frac{U_p U'_s}{2\pi f L_{\text{eq}}} \sin\varphi \tag{16}$$

where U_p and U'_s are rms values of the first harmonic of the primary voltage and of the secondary voltage taken to primary side, while φ is the phase-shift between the primary and secondary voltages. Controlling the power level and flow direction in this system is possible in several ways.

1) By varying the duty cycle of the inverters, values of the first harmonic of the primary and secondary inverters voltage will change, thus influencing the power level.
2) Changing the phase shift between the primary and secondary voltages changes both power level and direction of the power flow, thus in this way change between G2V and V2G modes of operation is achieved.
3) Operating frequency influences the equivalent reactance seen between the two sides, meaning that a change in frequency would cause a change in the power level. However, because of the narrow range of the operating frequencies for the considered application, the operating frequency will be fixed.

Considering that the system is intended for automotive charging applications, it is required that it remains operable and efficient under the wide range of operating conditions, out of which, the most important ones are the ones considering different clearance and misalignment conditions and different battery voltage levels. Duty cycle control will be used to compensate for the changes in the system caused by deviation of the system from the nominal condition, i.e., the conditions in which the ratio of the dc voltage levels of primary and secondary side corresponds to the transfer ratio defined in (7). Depending on the topology of the entire system, it may also be possible to vary the input voltage of the primary inverter, however, in this work we will consider it invariable. Control of the phase-shift will be used for achieving the desired power flow and switching between G2V and V2G modes of operation.

As the system is composed out of two physically separated parts, two microcontroller units (MCUs) are necessary, one to control the primary inverter and other to control the secondary inverter. Problem of synchronizing the two MCUs in IPT applications can be encountered in the literature [54], [55]. This problem is as well analyzed in our previous work [52], where a synchronization strategy based on the control of the secondary inverters current is proposed, that is free of any wireless communication between the primary and secondary MCUs. In this way, the IPT system is seen as a controllable current source that pumps current into the battery, while the pumped current is being equal to the reference one provided by the EVs BMS. This provides a possibility to implement any of the charging methods mentioned in Section I. As the BMS has the measurements of the battery voltage and current [56], to implement CV or CP charging methods only one control loop with a PI controller is to be added to the BMS, output of which is the current reference provided to the secondary MCU, given in Fig. 1. During the charging process, once the battery voltage reaches its defined maximum value, the CV charging period starts. During this period, the reference for the battery current is not provided directly by the BMS, rather by a PI controller with task of maintaining the battery voltage constant. Once the battery current drops below certain predefined value, it is considered that the battery is charged and the charging process is brought to a stop. Implementation of the pulsed-current and CC charging does not require any additional control loops. In this way, the considered system mitigates the complex hybrid structures mentioned in Section I as the way to achieve the desired charging method, rather it is achieved by the appropriate control of the given system.

B. V2G Mode of Operation

One of the key features of the proposed EV charging concept is the bidirectionality feature that is permitted by the employed converter topology. It is out of interest to analyze the behavior of the given system in the V2G mode of operation in order to gain a deeper insight on the functionality of the system.

First thing that can be noted from the Fig. 4, is that the coils are asymmetrically distributed in space, i.e., primary and tertiary coil are placed next to each other, while the secondary is placed further away, on-board the vehicle. Two different aspects of the system functionality are to be discussed: power transfer and system efficiency.

From the point of view of power transfer, system will not exhibit different behavior while functioning in V2G mode of operation. In the previous section, the three coupled inductors are equalized to an three-winding transformer. At the operating frequency, tertiary capacitor resonates with the self-inductance of the tertiary winding, leading to the equivalent circuit given in Fig. 3(c). The equivalent inductor is seen between the primary and secondary side, determining the power transfer between the two sides accordingly to (16). For certain values of first harmonic of the primary and secondary voltages, a certain phase-shift φ causes a consequential active power flow from grid to vehicle, with amplitude equal to P. If sign of the phase-shift is changed to $-\varphi$, according to (16), the power flow will consequentially change sign and the power P will be transferred from vehicle to grid. The asymmetric distribution of the coils does not influence the coexistence of the power flow that arises from (16), as this equation relies on the equivalent circuit of the system that is derived in Section II, where spatial distribution of the coils is not relevant for the derived model.

On the other hand, the influence on the system efficiency does exist. If system was made with tertiary capacitance tuned accordingly to (15), and with equal values of L_{eqp} and L'_{eqs} the system efficiency would be the same. However, for the reasons considered more thoroughly in the following section, the tertiary capacitor is to be tuned differently, causing different system efficiencies in G2V and V2G modes of operation. This issue will be discussed in Section III-D.

C. Parameters of the Considered System

In the following section, design of the previously described system will be analyzed. In the case of this work, the EV charger has the following parameters.

1) Nominal primary dc voltage and nominal EV battery voltage equal to 800 V. Battery voltage range is [610 V, 830 V].
2) Nominal power of the charger is 30 kW.
3) Litz wire is designed according to [57] and it is made out of 3000 strands of 70 μm diameter, yielding the current rating of 52 Arms assuming the current density of 4.5 A/mm^2, i.e., 58 A with the current density of 5 A/mm^2 that will be considered for the tertiary coil due to its size and position.
4) Outer diameter of the coil is 350 mm, as it is defined in the SAE standard [4], for the Z2 class of clearance range. Air gap between the GA and the vehicle assembly (VA) is varying between 110 and 150 mm (Clearance between 145 and 185 mm as defined in the SAE standard). Considered misalignment is Â± 50 mm in both x and y direction.
5) Efficiency requirements are as well taken from the SAE standard [4]. System is required to have efficiency larger than 85% in the aligned position and efficiency larger than 80% in the misaligned position. Over the alignment tolerance area, the charger has to be able to transfer at least 50% of the nominal power.

IV. Design of the Considered System

The goal of this Section is to outline the design procedure of the considered three-coil IPT system. Two criteria are main for the design: high efficiency of the system and low weight added to the vehicle. In order to facilitate the understanding of the design procedure, it will be done in five consecutive steps as follows.

1) Determining number of turns of the primary, secondary, and tertiary coils, N_p, N_s, and N_t.
2) The analysis of the system controllability and reactive power consumption by designing the L_{eq}.
3) Improving the system efficiency by eliminating higher harmonics–adding the external inductor.
4) Further improving of the efficiency by tuning of the tertiary capacitance.

5) Final assessment of the power transfer capability and efficiency of the system in the specified design space.

In the following procedure, there is the requirement for calculating system losses several times. Main system losses are composed out of

1) conduction losses in the IPT coils and resonant circuit;
2) conduction losses in the primary and secondary inverter;
3) switching losses in the primary and secondary inverter;

while the losses in the ferrite beds of the IPT coils have been neglected due to the low density of the magnetic flux. Losses are calculated using the following equations.

$$P_l = P_{cl} + P_{ip} + P_{is} \tag{17}$$

$$P_{cl} = I_p^2 R_p + I_s^2 R_s + I_t^2 R_t \tag{18}$$

$$P_{ip} = 2I_p^2 R_{ip} + A_p(I_{\text{poff}})f + B_p(I_{\text{pon}})f \tag{19}$$

$$P_{is} = 2I_s^2 R_{is} + A_s(I_{\text{soff}})f + B_s(I_{\text{pon}})f \tag{20}$$

where R_p, R_s, and R_t are the ac resistances at the switching frequency of the primary, secondary, and tertiary part of the resonant link, respectively. R_{ip} and R_{is} are resistances of the primary and secondary inverter, A_p, B_p, A_s, and B_s are the parameters that can be extracted from the datasheet of the semiconductors, dependent on the value of the turn-OFFand turn-ON current.

A. Determining N_p, N_s, and N_t

The design of the IPT coils dominantly determines the weight that is being added to the vehicle. This determines the place of the tertiary winding, fixing it to the ground assembly (GA), on top of the primary winding, as it is shown in Fig. 4. The winding is designed fixing the core geometry in accordance with the current standard proposal and the winding geometry is adjusted to obtain the maximum coupling factor [58]. The very topic of coil design is extensive, incorporates several different areas such as winding geometry, core geometry, Litz wire design, etc. Detailed procedure for coil design is given in [58, Chap. V]. In this work, we addressed directly only the topic of the number of turns of the windings, as it is the most important for the presented work. As we tend to keep the added weight minimal, the number of turns of the secondary coil is sought to be as low as possible. Equation (7) can be rewritten in the following way:

$$\frac{n_p}{n_s} = \frac{k_{pt}\sqrt{l_p}N_p}{k_{st}\sqrt{l_s}N_s} \tag{21}$$

where l_p and l_s are per-turn inductances of the primary and secondary coils, respectively, that have values determined by the geometry of the winding. From here it proceeds, that achieving a certain transfer ratio with a minimal number of turns on the secondary, requires that the primary winding is made with as low number of turns as possible. Limiting factor to the number of primary turns is the design of the tertiary coil. The VA rating of the tertiary coil is equal to

$$I_{t1}^2 \omega L_t = \frac{U_p^2}{k_{pt}^2 \omega L_p}. \tag{22}$$

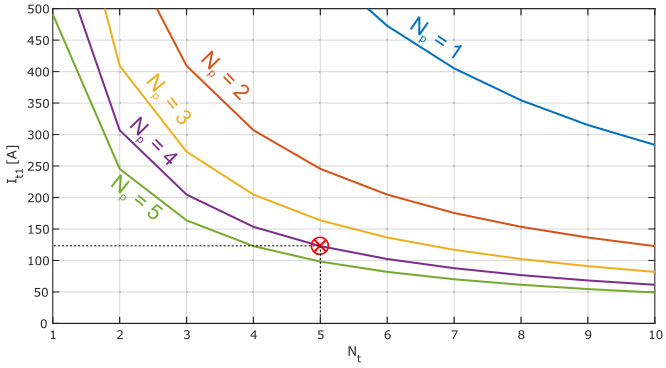

Fig. 5. First harmonic of the tertiary current in dependence on the number of turns of the tertiary, for different number of primary turns.

Problem with having a low value the of primary self-inductance L_p is that the required VA rating of the tertiary coil is consequently large. Design of such a coil depends mainly on the characteristics of the available Litz wire and the physical constraints such as the coil dimensions. Fig. 5 shows the dependence between the first harmonic of the tertiary current on the number of turns of the tertiary, for different number of turns of the primary coil. ANSYS Maxwell was used in this process for finite element analysis (FEA) of the considered system. Based on this data and the space available for the tertiary winding, tertiary winding is made with five turns, each turn being consisted out of three wires in parallel. Number of turns of the primary coil is 4. VA rating of the tertiary winding is 120 kVA. Current at the tertiary winding in the nominal condition is 127 A, leaving enough of the safety margin due to the potential difference between simulated values and real-life values and for the possible overcompensation of the tertiary that will be considered in Section IV-D. Number of turns of the secondary winding is determined based on the desired transfer ratio. From (7), it is clear that the transfer ratio will vary depending on the coupling conditions. Nominal transfer ratio is defined as the transfer ratio calculated according to (7), in the aligned case and air gap being equal to the mid-point from the considered range of air gaps. Nominal transfer ratio will be determined so that it is equal to the ratio between the input dc voltage and the EV battery voltage equal to the mid-point from the range

$$\left(\frac{n_p}{n_s}\right)_n = \frac{2V_{\text{in}}}{V_{\text{batt}}^{\min} + V_{\text{batt}}^{\max}}. \tag{23}$$

Equalizing right-hand sides of (21) and (23), one obtains the number of turns of the secondary coil. Using the FEA simulation to obtain per-turn inductances of the coils and the coupling factors between them, it is determined that the required number of turns on the secondary is 13. Parameters of the simulated system and of the equivalent circuit are given in Table I. With this, the design of the coils is concluded. Coils designed in the previously described manner, allow for high efficiency of the system through ensuring a wide range of operating conditions where zero-voltage-switching (ZVS) is achievable. This topic is discussed more in-detail in Section IV-E. From the point of view of coil design, Eq. (23) determines the number of turns of

TABLE I
SIMULATED PARAMETERS OF THE CONSIDERED THREE-COIL SYSTEM AND THE PARAMETERS OF THE EQUIVALENT CIRCUIT IN THE OPERATING POINT FOR WHICH THE SYSTEM IS DESIGNED

Parameter	Value	Parameter	Value
L_p [μH]	10.56	n_p/n_s	1.15
L_s [μH]	106.05	n_p/n_t	0.77
L_t [μH]	13.86	L_μ [μH]	8.18
L_{ps} [μH]	7.07	$L_{\gamma p}$ [μH]	2.38
L_{pt} [μH]	10.64	$L_{\gamma s}$ [μH]	99.86
L_{st} [μH]	9.191	$L_{\gamma t}$ [μH]	0.06

the secondary is crucial as the given transfer ratio is the main parameter that influences the range of system conditions where ZVS will be possible.

B. The Analysis of the System Controllability and Reactive Power Consumption by Designing the L_{eq}

Once that the IPT coils are defined it is necessary to determine the primary, secondary, and tertiary capacitor values. In order to do this, first, the value of the equivalent inductance L_{eq} has to be defined. Let us analyze the system using the equivalent circuit given in Fig. 3(c). The operating condition of the considered system we will call *ideal* if the rms values of the first harmonic of the primary voltage and of the secondary voltage taken to the primary side, U_p and U_s', are equal between themselves and in the same time equal to their maximum possible value. The system is said to operate in the *nominal* condition if the transfer ratio n_p/n_s is equal to its nominal value, while the system is transferring the nominal power P_n and working in the ideal condition. Phase-shift φ, and the equivalent inductance L_{eq} in the nominal condition are φ_n and L_{eqn}. For the system operating in the nominal condition, active power that is being transferred, reactive powers that are being given by the primary and secondary inverters and the one that is being consumed by the equivalent inductance are, respectively:

$$P_n = \frac{U_p U_s'}{2\pi f L_{\text{eqn}}} \sin\varphi_n \tag{24}$$

$$Q_p = \frac{U_p^2 - U_p U_s' \cos\varphi_n}{2\pi f L_{\text{eqn}}} \tag{25}$$

$$Q_s = \frac{U_s'^2 - U_p U_s' \cos\varphi_n}{2\pi f L_{\text{eqn}}} \tag{26}$$

$$Q_L = \frac{U_p^2 - 2U_p U_s' \cos\varphi_n + U_s'^2}{2\pi f L_{\text{eqn}}}. \tag{27}$$

From (24) and (27), introducing that $U_p = U_s'$, one obtains

$$Q_L = P_n \tan\frac{\varphi_n}{2}. \tag{28}$$

For the system to operate with the minimal reactive power it is clear, from Eq. (28). that it should be designed that in the nominal conditions $\varphi_n \to 0$. Under this condition, from Eq. (24), it follows that $L_{\text{eqn}} \to 0$ in order to have the nonzero, constant, power flow. This is the point where the first tradeoff is made. On the one hand, low values of L_{eqn} will cause low requirement for reactive power and low conduction losses. However, on the other side, if L_{eqn} is too small, small changes in phase-shift will cause big changes in the power level, thus system may become hard to control and inoperable. Fig. 6(a) depicts variation of active power with the phase-shift for different values of equivalent inductance, as well as the phase shift for which the certain reference power level is achieved. In the vicinity of the nominal operating point, change of power with a change in phase-shift is given with

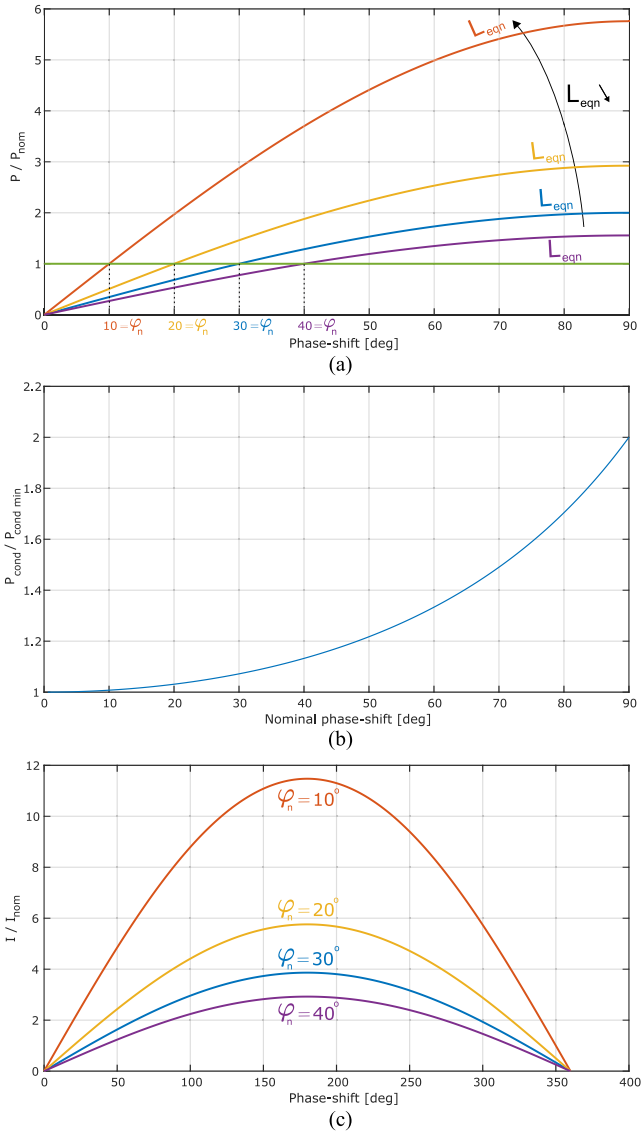

Fig. 6. (a) Change of power with change in phase-shift for different values of equivalent inductance. (b) Ratio between conduction losses ant the minimum conduction losses with change in phase-shift. (c) Ratio between current and nominal current at different phase-shifts, for different nominal phase-shift angles φ_n.

$$\frac{\mathrm{d}P}{\mathrm{d}\varphi} = P_n \cot\varphi_n. \tag{29}$$

Being that the operating frequency of the EV IPT chargers is between 80 and 90 kHz, mismatch in the phase-shift caused by a potential latency of 20–50 ns is between 1° and 2°. In order

to keep the potential drops or spikes in power level, caused by the small mismatch in phase-shift, between 2% and 3% of the nominal power, using Eq. (29), it is calculated that the nominal phase-shift should not be less than 30°. From Fig. 6(b), it is visible that, for this value of phase-shift, conduction losses increase caused by the reactive power are around 7%, which is acceptable. Furthermore, from the value of L_{eqn} depends the value of potential overcurrent, caused by the synchronism failure between the primary and secondary converters. The value of this current at the primary side, under nominal conditions is calculated using

$$|I_n| = \frac{U_p}{2\pi f L_{\text{eqn}}} \sqrt{(\cos\varphi_n - 1)^2 + \sin^2\varphi_n}. \tag{30}$$

This dependency is shown in Fig. 6(c). If the equivalent inductance is designed in a way that the referenced power is achieved for the proposed phase-shift value of 30°, in the case of synchronism failure, maximum overcurrent is approximately equal to four times the nominal current. This is the value that contemporary SiC MOSFET transistors can endure for certain amount of time, so the protection circuit of the converters has time to react and prevent the damage. So, the value of L_{eqn} is calculated using

$$L_{\text{eqn}} = \frac{U_p U_s'}{4\pi f P_n}. \tag{31}$$

To have a perfect symmetry between the primary and secondary sides in nominal conditions, values L_{eqp} and L'_{eqs} from Fig. 3(c) are chosen to be equal to half of the equivalent inductance L_{eqn}. Based on the previous discussion, the initial values of the primary, secondary, and tertiary capacitors for the following iterative process are determined according to the (13)–(15).

C. Improving the System Efficiency by Eliminating Higher Harmonics–Adding the External Inductor

Due to the low values of the self-inductances of the coils, it is necessary to check for the higher harmonic components in the primary and secondary currents. Circuit from Fig. 3(a) is linear and can easily be solved either numerically or using some circuit simulator software. For the sake of simplicity, we will omit writing the differential equations describing the system from Fig. 3(a). On Fig. 7(a) the waveforms of the primary and secondary currents and voltage obtained using PLECS are shown. rms of the primary and secondary currents are 50.2 and 51.4 A, while the instantaneous values of the primary and secondary currents in the switching transitions are, respectively, 70 and 26.4 A. As it can be seen, the current in the switching moment in the primary inverter is substantial due to the influence of higher harmonic components in the primary current. Adding an external inductance to the primary, while keeping the same equivalent inductance by adapting the capacitance values, is the most simple way to reduce the higher harmonic currents in the primary.

The chosen value of the added inductor depends on the permissible switching current and available space. Clearly, the higher the added inductance value is, the higher current harmonics will be suppressed more, however, the size of the added

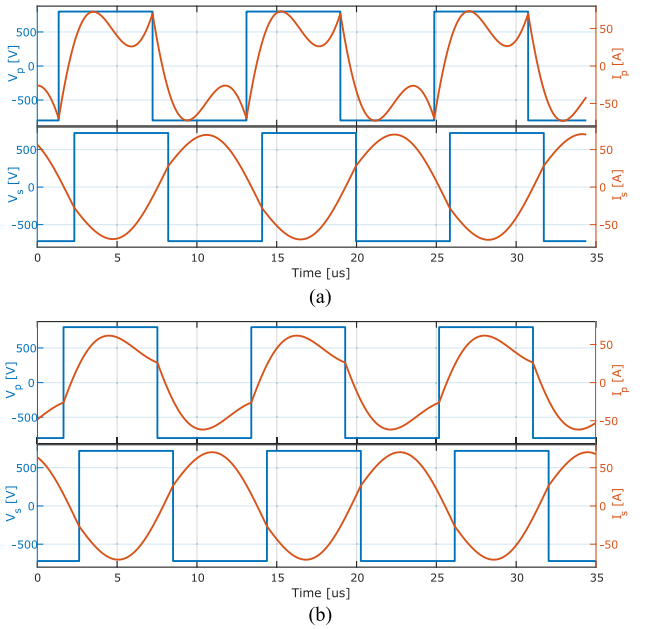

Fig. 7. (a) Primary inverter voltage and current and secondary inverter voltage and current with $L_{addp} = 5.72$ μH and $C_s = 37.4$ nF (b) Primary inverter voltage and current and secondary inverter voltage and current with $L_{addp} = 30$ μH, $C_p = 144.5$ nF and $C_s = 37.4$ nF.

inductor represents a limiting factor. In this work, we have chosen to add an inductor of 30 μH. Simulated voltages and currents in this case are given in Fig. 7(b). Comparing this to the case shown in Fig. 7(a), rms of the primary and secondary currents are 44.6 and 50.5 A, while the instantaneous values of the primary and secondary currents in the switching transitions are, respectively, 26.6 and 26.4 A.

By now, the influence of the higher harmonic current has been suppressed in the overall rms of the primary and secondary currents; however, it still has some influence in the switching current, i.e., the switching losses.

D. Further Improving of the Efficiency by Tuning of the Tertiary Capacitance

In the previous calculus, value of the tertiary capacitance was calculated according to (15). However, it is possible that the total system losses can be reduced more by varying the value of the tertiary capacitance. In case that the tertiary circuit is out of resonance at the fundamental frequency, i.e., it is injecting (capacitive behavior–tertiary is overcompensated) or draining (inductive behavior–tertiary is undercompensated) reactive power, the equivalent circuit or the system can be represented using an equivalent Π schematic given in Fig. 8. Parameters of the Π schematic are defined using the following equations:

$$L_{\text{eq}}^{\Pi} = L_{\text{eqp}} + L'_{\text{eqs}} + \frac{\omega^2 L_{\text{eqp}} L'_{\text{eqs}}}{Z_{\text{eq}}} \tag{32}$$

$$Z_{\text{eqp}}^{\Pi} = \omega L_{\text{eqp}} + Z_{\text{eq}} + \frac{L_{\text{eqp}}}{L'_{\text{eqs}}} Z_{\text{eq}} \tag{33}$$

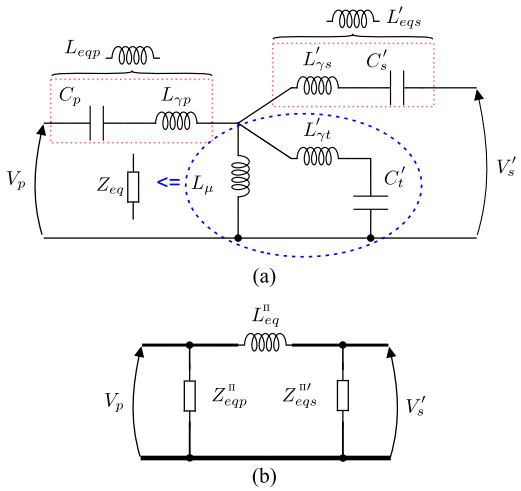

Fig. 8. (a) T equivalent circuit of the three-coil system with overcompensated tertiary winding. (b) Π equivalent circuit of the considered three-coil system.

$$Z^{\Pi'}_{\text{eqs}} = \omega L'_{\text{eqs}} + Z_{\text{eq}} + \frac{L'_{\text{eqs}}}{L_{\text{eqp}}} Z_{\text{eq}}. \tag{34}$$

First, the losses are calculated. Depending what losses are dominant, C_t is to be increased or decreased. If the conduction losses in the tertiary circuit are dominant, C_t should be decreased. If the converter losses are dominant, C_t should be increased. C_p and C_s are recalculated each time in order to keep L^{Π}_{eq} constant. The iterative process is maintained until the total losses start rising. The final values of the capacitors are C_p =144.4 nF, C_s =37.4 nF, and C_t =274 nF. The proposed capacitor tuning method differs from all of the tuning methods mentioned in Section I as it leads to having an equivalent inductance seen between the primary and secondary sides, while most of the tuning methods from the cited works strive to achieve a resonance independent on the coupling between the coils, thus they tend toward the well-known gyrator structure via tuning the compensation capacitors to resonate with the self-inductances of the coils. The estimated efficiency of the system is more than 96% for the inverters made with G3R20MT12 N transistors and for the estimated ac resistances of the primary, secondary, and tertiary parts of the circuit, respectively, equal to 40, 140, and 20 mΩ. The resistances were estimated using the methodology based on the homogenization of the Litz wire conductor and simulations in FEA software. This methodology was employed for the resistance estimation in our previous research activity, where the same Litz wire was employed [57], [57], [59]. The estimated primary resistance includes for the added inductor as well. As the result of increasing the tertiary capacitance, current in the tertiary winding is increased to the 152 A and its VA rating as well to 171 kVA.

Throwing the tertiary capacitor out of resonance will reflect itself through different efficiencies of the system in G2V and V2G modes of operation. Namely, solving the circuit from Fig. 8(b), the primary and secondary inverter currents will be different, causing different losses in the inverters. Also, the losses in the tertiary winding will be different due to the different voltage

TABLE II
SIMULATED PARAMETERS OF THE CONSIDERED THREE-COIL SYSTEM AND THE PARAMETERS OF THE EQUIVALENT CIRCUIT FOR THE CLEARANCE OF 160 MM AND MISALIGNMENT IN BOTH *X*- AND *Y*-AXES EQUAL TO 50 MM

Parameter	Value	Parameter	Value
L_p [μH]	10.62	n_p/n_s	1.96
L_s [μH]	104.4	n_p/n_t	0.77
L_t [μH]	13.92	L_μ [μH]	8.26
L_{ps} [μH]	4.22	$L_{\gamma p}$ [μH]	2.36
L_{pt} [μH]	10.69	$L_{\gamma s}$ [μH]	102.251
L_{st} [μH]	5.46	$L_{\gamma t}$ [μH]	0.06

seen at the magnetizing inductance that is shown in Fig. 3(c). The different voltage in two cases is caused by different inverter currents.

E. Final Assessment of the Power Transfer Capability and Efficiency of the System in the Specified Design Space

In order to verify the proposed design, it is necessary to check whether the previously designed system complies with the design goals defined in the beginning. So, in the case of this work, the questions are as follows.

1) Is the system capable to transfer the minimum power that is required of it in all of the possible conditions?
2) Is the efficiency of the system sufficiently high in all of the possible conditions?

To check the first question, it is necessary to simulate the system in the position with maximal clearance and misalignment. Simulated parameters are given in Table II. In terms of power transfer capability, critical is the case with the minimal voltage of the EV battery. In the discussed case, the maximal power that can be transferred is equal to

$$P_{\text{max}} = \frac{U_p U'_{s\text{min}}}{2\pi f L_{\text{eq}}}. \tag{35}$$

Introducing the system parameters and the parameters from Table II into the previous equation, for the designed system, it is obtained that the P_{max} equals to 35.02 kW. However, due to the Litz wire current limitation of 52 A on the secondary side, power is limited to a lower value. The matter of efficiency under various clearance values and alignment conditions is important as well. To analyze the system behavior under the misalignment and varying air gap conditions, a parameter called *relative coupling coefficient* is introduced, designated with ξ. This parameter basically represents a metric of measuring the coupling of the coils of the transmitter (primary and tertiary) with the coil of the receiver (secondary). Due to the position and sizes of the coils, it is valid to claim that the mutual inductances L_{ps} and L_{st} will change proportionally respective to their nominal values with the same scaling coefficient, with the change of the secondary coils position. The scaling coefficient, that quantifies the ratio between the L_{ps} and L_{st} in the nominal condition and their corresponding values in some other position of the secondary is the previously mentioned ξ, i.e.,

$$L_{\text{ps}} = \xi L_{\text{psn}} \tag{36}$$

$$L_{\text{st}} = \xi L_{\text{stn}} \tag{37}$$

where L_{psn} and L_{stn} are nominal values of the corresponding mutual inductances, that can be seen in Table I. In the nominal position ξ equals to one. Using ANSYS Maxwell, it is possible to validate that in the considered design space defined at the end of the previous section, ξ is in range between 0.6 and 1.3. Through this, the convenience of the introduced parameter ξ is reflected, as the system will exhibit the same behavior for various air-gaps and alignment positions, as long as the considered positions have the same value of the parameter ξ. This means, that the control of the system will depend on the parameter ξ, and not on the air-gap and alignment, as the information about these two parameters is contained in the ξ. Variation of the L_{ps} and L_{st} over the alignment area, influences the transfer ratio from the (7) and the secondary leakage inductance from (11). Thus, it changes the parameters L'_{eqs} and U'_s from Fig. 3(c). As the certain power level can be transferred for various different values of primary and secondary inverter duty cycles, each combination having a different phase-shift, finding the optimal working point of the system under nonnominal conditions is not an easy problem. However, it is always possible to fix one of the inverter duty cycles. If ξ is lower than 1, than the duty cycle of the primary is kept constant, while the duty cycle of the secondary is reduced. In the case when the ξ is bigger than 1, it is done otherwise. In CV charging mode, as the transferred power is gradually reducing, so it is beneficial to reduce both duty cycles, as this will lead to reduction in the current of the tertiary winding. Equivalent circuit from Fig. 8(b) has been analyzed for different values of the parameter ξ. For calculating the losses, same parameters as in the previous section are used. Systematic circuit simulations using PLECS are conducted in order to obtain the relevant parameters of the circuit such as the rms of the currents and the currents in switching transitions. For the values of ξ in the given range, battery voltage, power level, and duty cycles of the inverters are varied to find the optimal working point for each of the possible cases of relative coupling coefficient and battery voltage levels. Expected efficiency of the system is between 90% and 97% considering all conditions. Nominal power of 30 kW is possible to achieve under higher battery voltage levels and with the higher relative coupling coefficient. For this reason, CC/CV charging method would be the most appropriate for the proposed charger topology, as it naturally requires lower power with lower battery voltages.

Hidden under the previously described method of finding the optimal operating conditions of the system for each value of ξ from the considered range, is the discussion about switching of the semiconductors. Namely, ZVS is a very important feature of the system, from the point of view of having high-efficiency and low electromagnetic interference (EMI). The inductive nature of the impedance seen between the primary and secondary contributes positively to the ZVS, as well as do the higher harmonic components in the inverter currents. As the loss of ZVS leads to significant increase in switching losses, the previously described method is naturally going to select cases with ZVS as optimal for the system operation whenever it is possible to achieve ZVS. The possibility of achieving ZVS depends on three factors: the relative coupling coefficient ξ, battery voltage, and power that is being transferred. Fig. 10 shows the dependency of switching conditions on the ξ and battery voltage for the given power level of 30 kW. In the same figure, it is possible to visualize the systems capability to transfer the nominal power under different coupling conditions and battery voltages being that these two parameters are the ones determining the systems power transfer capability. Approximately, for $\xi \geq 0.8$ system is able to transfer the nominal power.

The expected efficiency of the system is higher than it is required by the SAE standard [4], thus it can be proceeded

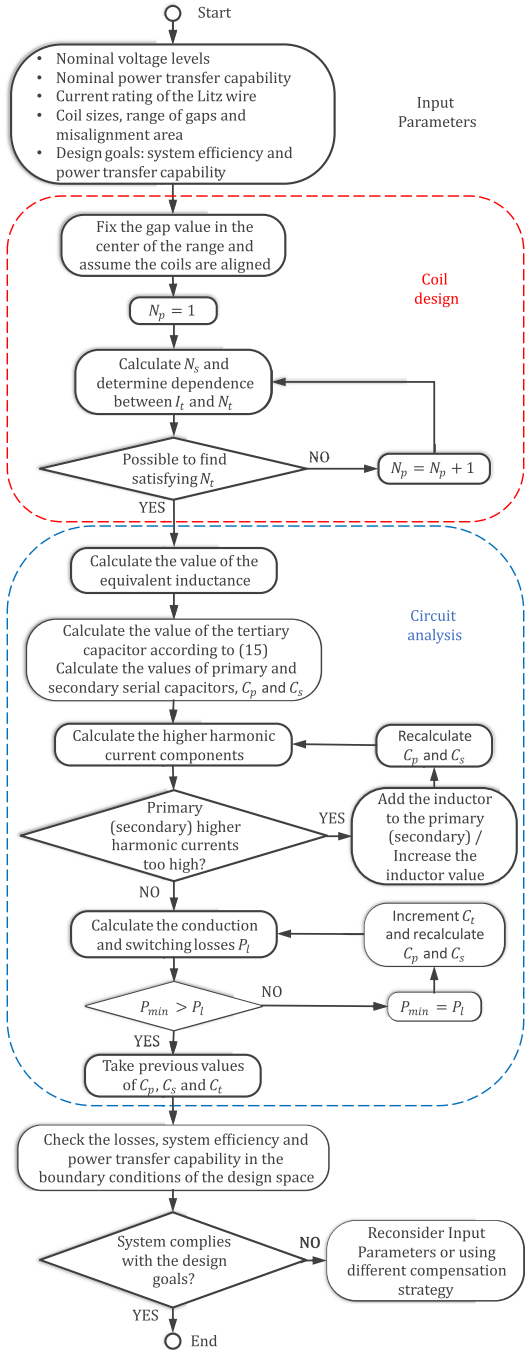

Fig. 9. Design flowchart.

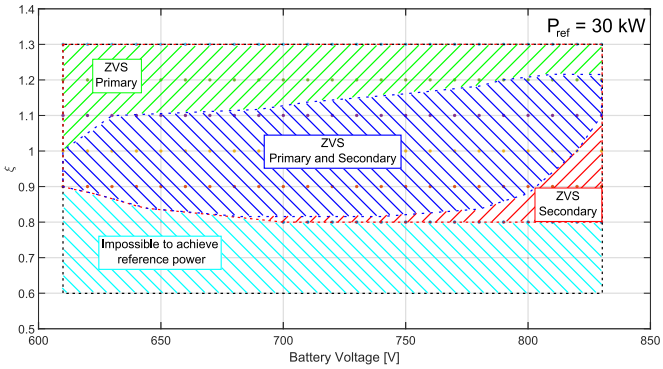

Fig. 10. Area depicting possibility of achieving ZVS for 30 kW of power being transferred.

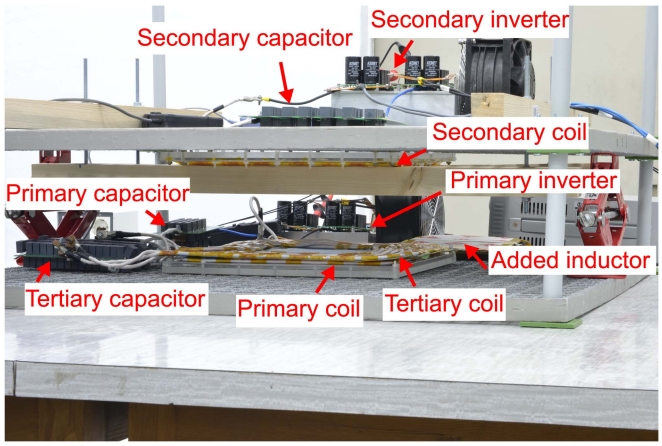

Fig. 11. Experimental setup.

with the prototype building and testing procedures. The entire design process described in this section can be represented using a flowchart given in Fig. 9.

V. Experimental Results

A. Testing of the Tertiary Coil

Experimental setup built to verify the ideas proposed in this work is given in Fig. 11. Detailed look of the primary, secondary, and tertiary coils is given in Fig. 12. The number of turns of each winding is 4, 13, and 5, respectively. Thickness of the ferrite core is 5 mm. The tertiary winding shown in Fig. 12(c) is made with three wires in parallel. In order to prevent circulating currents in the tertiary winding and the consequential reduction in the system efficiency, the conductors are interleaved in the way that in each turn, each of the three conductors, takes each of the three positions for one third of the turn length. In this way, the symmetricity of the conductors composing the tertiary winding is achieved. Fig. 13 shows the tertiary current waveforms measured in each of the three conductors of the tertiary winding, and the one measured as the sum of the three. The test was conducted with the open secondary coil and with the primary full-bridge generating a square-wave voltage with 50% duty cycle at half of its nominal voltage. As it can be seen, the currents in the

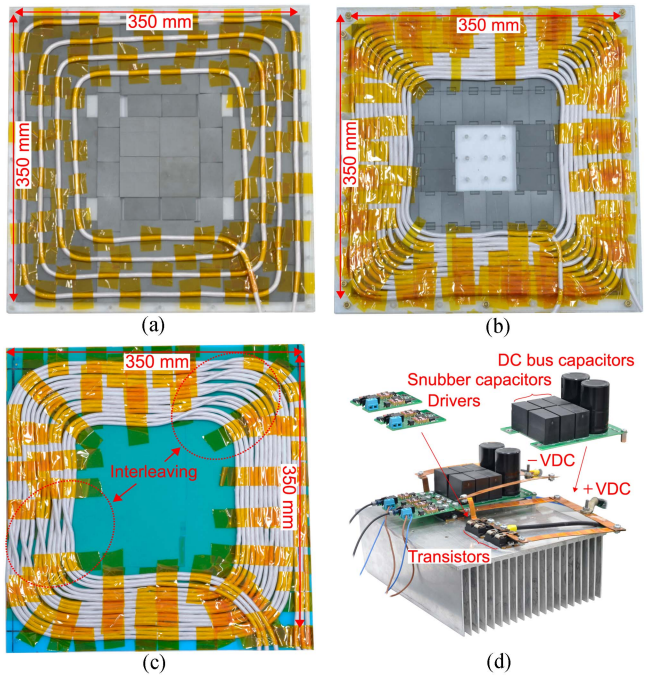

Fig. 12. (a) Primary coil. (b) Secondary coil. (c) Tertiary coil. (d) Inverter.

three conductors of the tertiary winding are well balanced as intended. Total rms current in the tertiary winding is equal to 84.85 A, yielding that with the nominal primary voltage it will be twice as much, giving the maximum predicted current density of 5 A/mm^2 in the tertiary conductors and the total power of the tertiary coil of 229 kVA.

The 10% higher current than simulated is the consequence of the 10% difference in the tertiary winding inductance comparing to the simulations. This is the worst case scenario as there is no power transfer so the voltage on the magnetizing inductance from Fig. 7(a) is maximal. When transferring power, this current will be lower due to the voltage drop on the equivalent primary inductance.

B. CC/CP Charging

A series of tests are conducted in order to test the claims given in this work. The system was tested in three significant positions, where the simulated value of the relative coupling coefficient ξ is equal to 0.6, 1, and 1.3. In Table III, measured parameters of the system in all of the three considered cases are given. In each of the cases, system was first tested both using the CP and CC charging methods. Table IV shows the summarized data of the CP and CC conducted tests. The power for CP charging is chosen in a way that it is possible to be reached for all of the battery voltages from the considered range. The current at the secondary coil will be highest when the battery voltage is lowest, and it is this case that determines the maximum power for CP charging. On the other hand, with the CC charging method, charging power increases with the increase in battery voltage. In both cases, the limiting factor is the rated current of the primary and secondary coils, as they are limited by the conditions given in the end of

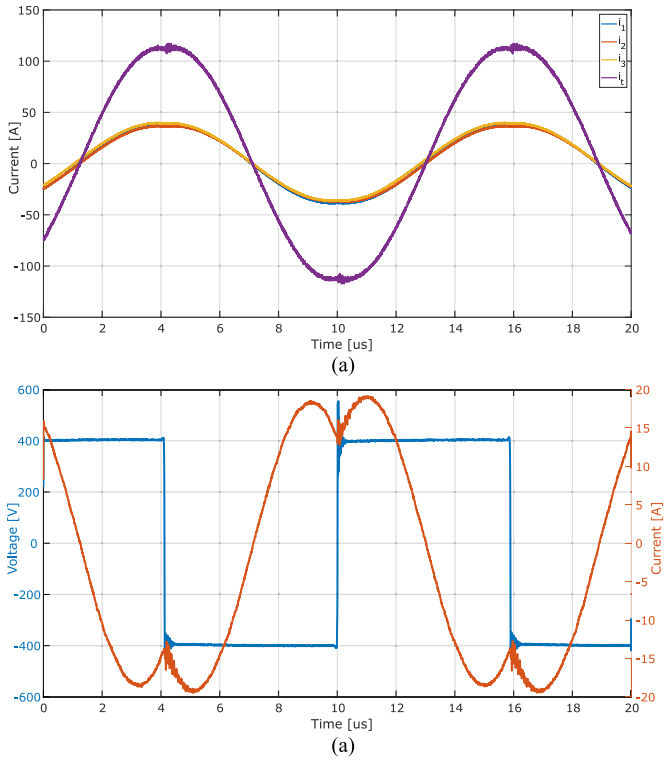

Fig. 13. (a) Measured currents in the three conductors of the tertiary winding and the total current. (b) Voltage and current of the primary inverter.

TABLE III
MEASURED PARAMETERS OF THE SYSTEM IN THE THREE TESTED CONDITIONS

Parameter	$\xi_{\text{sim}} = 1.3$	$\xi_{\text{sim}} = 1$	$\xi_{\text{sim}} = 0.6$
Air gap	110 mm	130 mm	150 mm
Clearance	145 mm	165 mm	185 mm
Misalignment (x,y)	(0 mm,0 mm)	(0 mm,0 mm)	(50 mm,50 mm)
ξ_{meas}	1.27	0.99	0.62
L_p [μH]	11.49	11.49	11.49
L_s [μH]	105.43	105.67	105.81
L_t [μH]	14.89	14.89	14.89
L_{ps} [μH]	8.98	7.2	4.38
k_{ps}	0.258	0.207	0.126
L_{pt} [μH]	10.99	10.99	10.99
k_{pt}	0.84	0.84	0.84
L_{st} [μH]	11.35	8.94	5.54
k_{st}	0.286	0.226	0.140

Section III. The charging times using the CP and CC charging methods as the later one has higher average power delivered to the EV battery.

First, the test with the highest relative coupling coefficient is conducted. In CP charging mode, it is tested for the power transfer of 30 kW. For the variation of the battery voltage in the entire range between 610 and 830 V, the system efficiency was between 95.75% and 96.54% and the battery current was between 36.14 and 49.12 A. Current and voltage waveforms of the primary and secondary inverters in this case are given in Fig. 14(a)–(c), for battery voltage levels of 610, 710, and 830 V, respectively. CC charging was done with two different values of the charging current, 34 and 45 A. In the first case of CC charging, system efficiency was between 95.91% and 96.52%, while the charging power was between 20.7 and 28.2 kW. In the second case, system efficiency was between 95.86% and 96.72% and the charging power was between 27.5 and 37.4 kW. Currents and voltages of the primary and secondary inverters, for this case, are given in Fig. 14(d)–(f). As it can be seen from the given data, CC charging is more appropriate for this charger type as it allows for higher power transfer with higher battery voltage levels, thus confirming the statement given in the previous section.

In the second position in which the system was tested, for $\xi = 0.99$, same tests as with $\xi = 1.27$ are conducted. In CP charging mode the system is tested for 30 kW power level. Measured efficiency of the system was between 95.82% and 96.35%, while the charging current varied between 36.14 and 49.12 A. Fig. 15(a)–(c) depicts the voltage and current waveforms for the battery voltage levels of 610, 710, and 830 V. Charging the battery with constant current equal to 34 A is analyzed next. Measured efficiency of the system in this case was between 95.72% and 95.93%, while the charging power was between 20.7 and 28.2 kW. Case where the battery is charged with the constant current of 45 A is shown in Fig. 15(d)–(f). Achieved system efficiency was between 95.85% and 96.35%, while the charging power was between 27.5 and 37.4 kW.

In the case, where the relative coupling coefficient ξ is equal to 0.62, i.e., when both the clearance and misalignment are maximal, it is not possible to transfer the nominal power in the entire considered voltage range of the battery. For that reason, the system is tested in the CP charging mode with the power level of 21 kW that is achievable for all of the battery voltage between 610 and 830 V. Fig. 16(a)–(c) shows the currents and voltages of the primary and secondary inverters during these tests, in the three characteristic points of the battery voltage interval. System efficiency was in range between 93.63% and 94.82%, while the battery current was in between 25.30 and 34.43 A. Fig. 16(d)–(f) depicts the relevant waveforms under CC charging test, where the battery voltage was equal to 610, 710, and 830 V, respectively, and the battery current was equal to 34 A. The efficiency of the system in these tests was in range between 94.04% and 94.82%, while the charging power varied between 20.7 and 28.2 kW. Fig. 17 gives the measured system efficiency curves for different battery voltage levels and in different cases of CC and CP charging that were tested.

Fig. 19 shows the losses breakdown in the nominal case, as defined in Section IV, that is shown in Fig. 15(b). Input voltage is 800 V, battery voltage is equal to 710 V, the relative coupling coefficient ξ is equal to 1, while the power being transferred to the EV battery is equal 30 kW. As it can be seen, dominant are the conduction losses in the tertiary winding. Due to its position and size, the tertiary winding makes a convenient place to concentrate the system losses as it is purely passive element with relatively big dissipation area. Yet, if these losses were mitigated to the inverter bridges, it would require them to have better cooling and would cause lower system efficiency as the resistance of one of the semiconductors is higher than the entire resistance of the tertiary circuit, thus justifying for the proposed solution of having high tertiary current and concentrating the losses there. Also, the key to maintaining the high

TABLE IV
OVERVIEW OF THE CP AND CC CONDUCTED TESTS AND RESULTS

ξ	Constant Power Charging			Constant Current Charging		
	Battery Current	System Efficiency Range	Charging Power	Battery Current	System Efficiency Range	Charging Power
1.27	36.14 A–49.12 A	95.75%–96.54%	30 kW	34 A	95.91%–96.52%	20.7 kW–28.2 kW
				45 A	95.86%–96.72%	27.5 kW–37.4 kW
0.99	36.14 A–49.12 A	95.82%–96.35%	30 kW	34 A	95.72%–95.93%	20.7 kW–28.2 kW
				45 A	95.85%–96.35%	27.5 kW–37.4 kW
0.62	25.30 A–34.43 A	93.63%–94.82%	21 kW	34 A	94.04%–94.82%	20.7 kW–28.2 kW

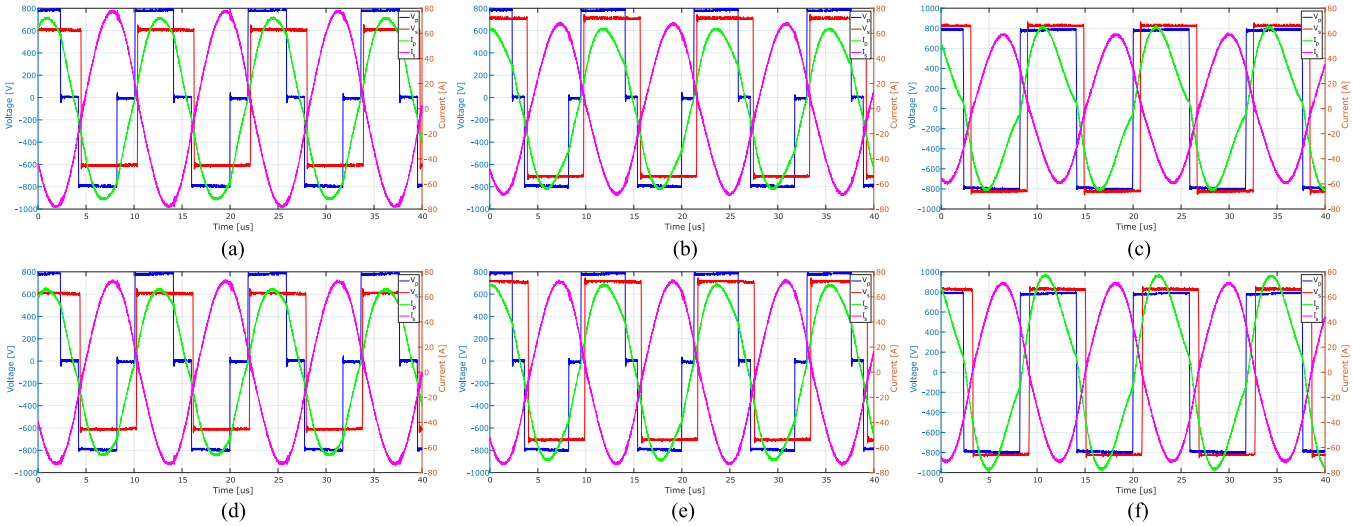

Fig. 14. Currents and voltages of the primary and secondary inverters for $\xi = 1.27$, (a) $V_{\text{batt}} = 610$ V, $P = 30$ kW (b) $V_{\text{batt}} = 710$ V, $P = 30$ kW (c) $V_{\text{batt}} = 830$ V, $P = 30$ kW (d) $V_{\text{batt}} = 610$ V, $I = 45$ A (e) $V_{\text{batt}} = 710$ V, $I = 45$ A (f) $V_{\text{batt}} = 830$ V, $I = 45$ A.

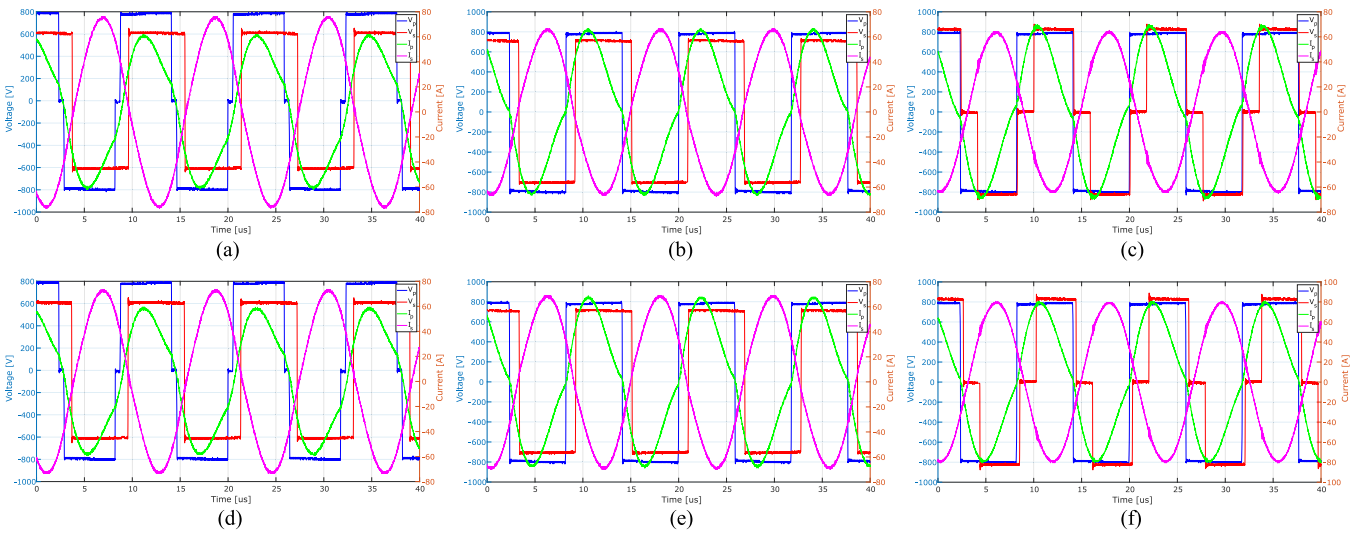

Fig. 15. Currents and voltages of the primary and secondary inverters for $\xi = 0.99$, (a) $V_{\text{batt}} = 610$ V, $P = 30$ kW (b) $V_{\text{batt}} = 710$ V, $P = 30$ kW (c) $V_{\text{batt}} = 830$ V, $P = 30$ kW (d) $V_{\text{batt}} = 610$ V, $I = 45$ A (e) $V_{\text{batt}} = 710$ V, $I = 45$ A (f) $V_{\text{batt}} = 830$ V, $I = 45$ A.

system efficiency during the following CV charging is to reduce the tertiary current by reducing the primary and secondary duty cycles as it will be shown. Cooling of the tertiary winding in the prototype was air-forced. In the case of having primary and tertiary coils encapsulated, it would be necessary to devise a ventilation system to guide the air inside the structure and to allow for the required cooling conditions.

C. CV Charging

After CC and CP charging test, efficiency of the system was examined under CV charging conditions, being that it is present both in CC/CV and CP/CV charging methods, in the second half of the battery charging process. Table V summarizes the CV charging results. System was tested with the same relative coupling coefficients as in the previous tests. Battery voltage was

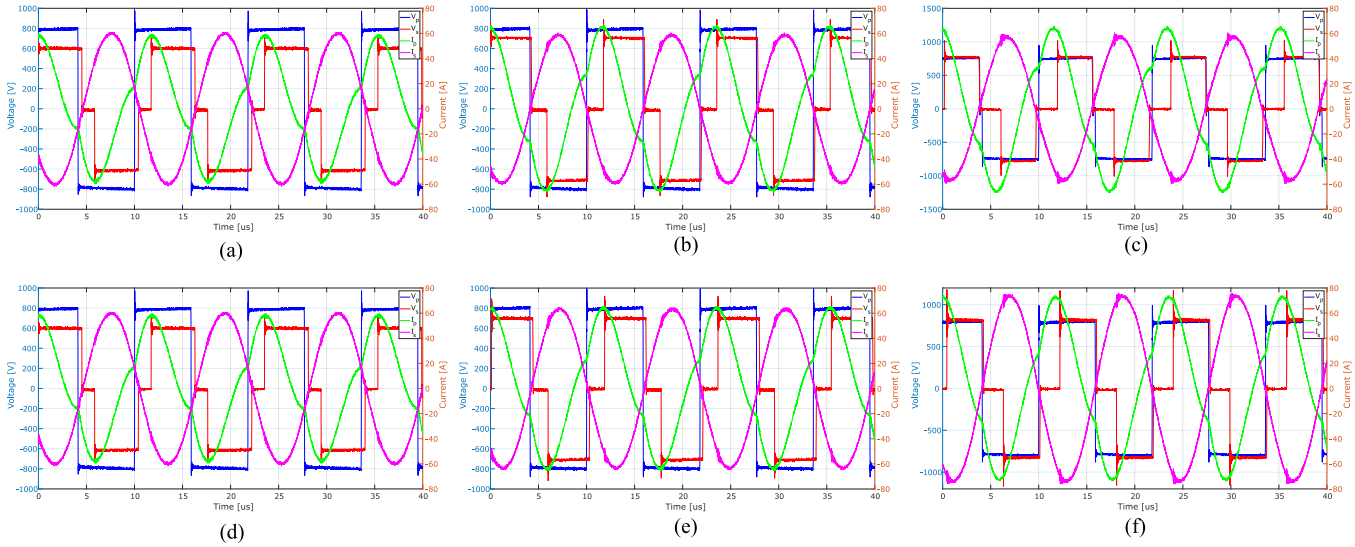

Fig. 16. Currents and voltages of the primary and secondary inverters for $\xi = 0.62$, (a) $V_{\text{batt}} = 610$ V, $P = 21$ kW (b) $V_{\text{batt}} = 710$ V, $P = 21$ kW (c) $V_{\text{batt}} = 830$ V, $P = 21$ kW (d) $V_{\text{batt}} = 610$ V, $I = 34$ A (e) $V_{\text{batt}} = 710$ V, $I = 34$ A (f) $V_{\text{batt}} = 830$ V, $I = 34$ A.

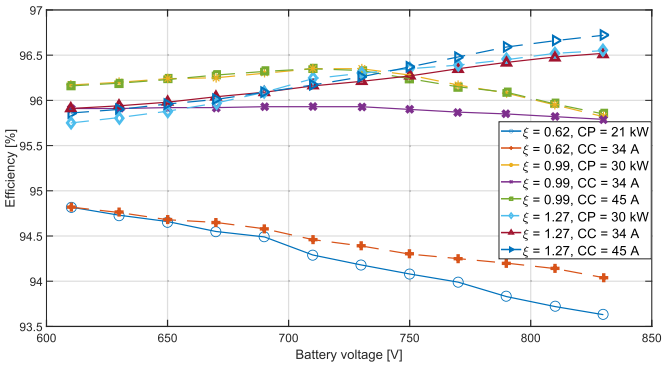

Fig. 17. System efficiency in CC and CP charging tests.

TABLE V
OVERVIEW OF THE CV CHARGING RESULTS

ξ	Constant Voltage Charging			
	Battery Voltage	Battery Current	System Efficiency Range	Charging Power
1.27	830 V	4.5 A–45 A	92.22%–96.72%	3.7 kW–37.5 kW
0.99	830 V	4.5 A–45 A	91.95%–95.85%	3.7 kW–37.5 kW
0.62	830 V	4.5 A–34 A	91.29%–94.04%	3.7 kW–28.2 kW

kept constant at 830 V while the battery current was changing between the maximum for each of the given cases, and the 10% value of the maximum current of 45 A, below which when the current drops, we consider that the battery is fully charged.

Fig. 18(a) and (b) shows relevant waveforms of the system for the case with the relative coupling coefficient equal to 1.27 during the CV charging part of the process, in two instants when the battery current is equal to 20 and 4.5 A, respectively. Case with the battery current equal to 45 A is already given in Fig. 14(g). System efficiency decreased together with the decrease in battery voltage, ranging from 96.72% to 92.22%, while the charging power changed from 37.5 to 3.7 kW.

In Fig. 18(c) and (d), analogously to the previous case, currents and voltages are given for the case of $\xi = 0.99$. Efficiency of the system decreased from 95.85% to 91.95%, while the change in the charging power is the same as in the previous case. Fig. 18(e) and (f) shows the waveforms for the case with minimal relative coupling coefficient. Case with the maximal charging current of 34 A in this case is given in Fig. 14(f). As the charging current decreased from 34 to 4.5 A in

this case, the system efficiency decreased from 94.04% to 91.29%, while the charging power decreased from 28.2 to 3.7 kW. Fig. 20 shows the variation of system efficiency with the change in battery current during the CV charging period, for the three previously discussed cases. All of the efficiencies measured in this work were obtained by utilizing the internal measurements of the Regatron programmable dc sources that were used for energizing the system.

Although the primary and secondary currents get distorted in the CV charging process due to higher presence of harmonics in the primary and secondary voltages, tertiary current will remain sinusoidal as its first harmonic is dominant due to the impedance characteristic of the circuit given in Fig. 8(a).

D. Thermal Considerations

Overall system losses in the nominal condition are given in Fig. 19. As it can be seen, the losses in the tertiary winding are dominant. While testing the presented prototype, air-forced cooling with 700 LFM was used for refrigerating the coils of the GA, mainly the tertiary coil. The temperature of the hottest point of the tertiary winding reaches 94 °C in steady-state. Although high, this is still far away from the 180 °C limit of the isolation of the used Litz wire. This is, thermally, the most critical part of the system. As for the inverters, same air-forced cooling as for the

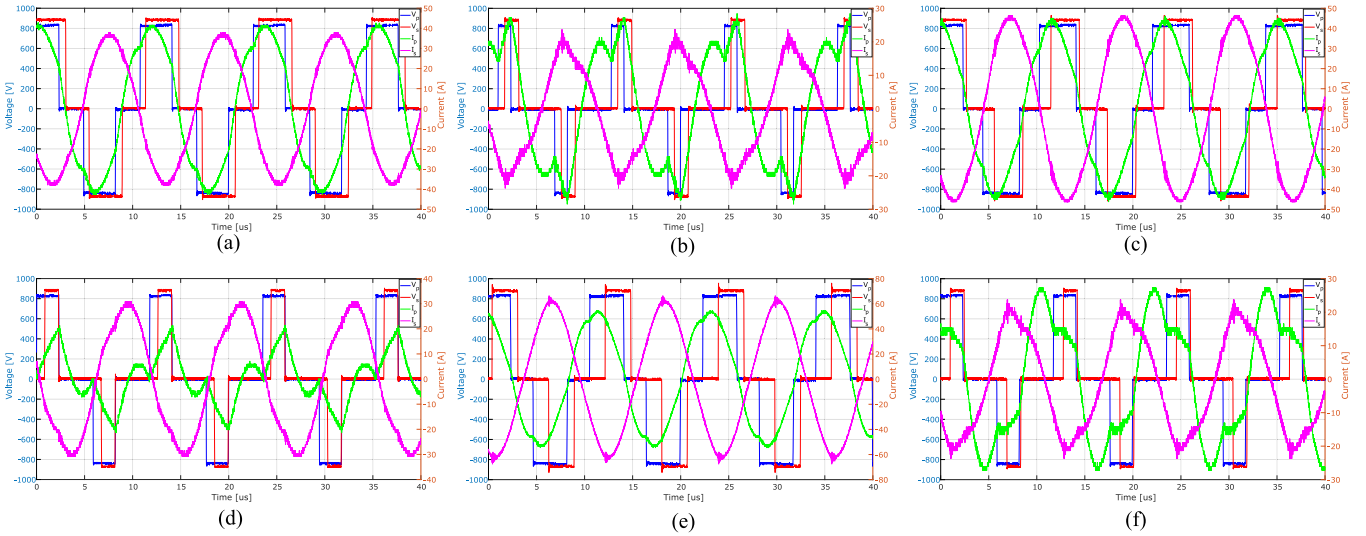

Fig. 18. Currents and voltages of the primary and of secondary inverters in CV charging mode for battery voltage equal to 830 V (a) $\xi = 1.27$ $I = 20$ A (b) $\xi = 1.27$ $I = 4.5$ A (c) $\xi = 0.99$ $I = 20$ A (d) $\xi = 0.99$ $I = 4.5$ A (e) $\xi = 0.62$ $I = 20$ A (f) $\xi = 0.62$ $I = 4.5$ A

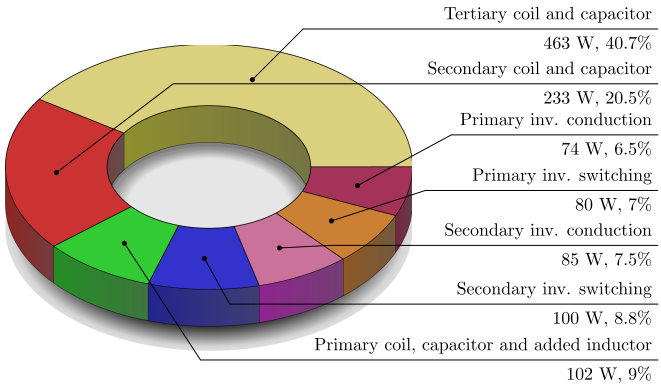

Fig. 19. Losses breakdown in the nominal condition.

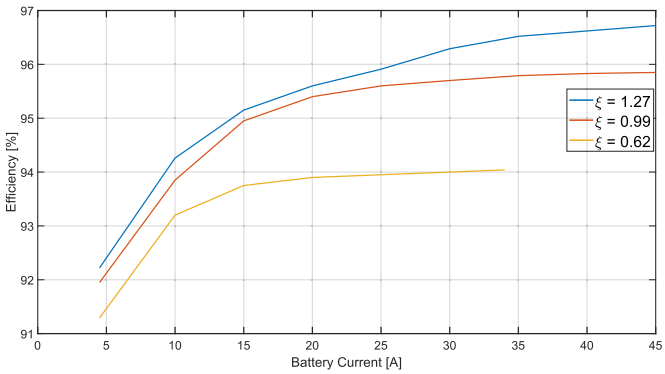

Fig. 20. System efficiency in CV charging tests.

GA was used. The transistors were placed on top of the heatsink as shown in Fig. 12(d). The thermal resistance between the case of the transistor and the ambient is, approximately, 0.15 °C/W. In the steady-state, while operating in the nominal point, under the given cooling conditions, the measured temperature of the case reaches 52 °C which is, having in mind the thermal resistance between junction and case from the datasheet of the used transistors, far under the limit for SiC technology.

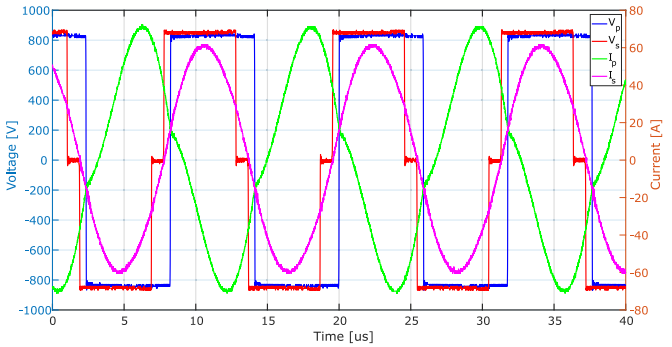

Fig. 21. System operating in V2G mode of operation.

E. Comparison to Other Works and V2G Test

Table VI gives the comparison between this work and the other relevant ones that were mentioned in the analysis of the state-of-the-art in Section I. As it can be seen, in terms of power level it is significantly higher than other cited articles. As for the system efficiency, it is in the top of the class, as are [30] and [17]. Out of all of the cited works, it is the only one that provides bidirectionality feature of the system. Misalignment is considered, as it is the crucial thing for EV charging applications.

To conclude the testing of the system, V2G mode of operation is checked. This mode of operation was checked for $\xi = 0.99$ and for battery voltage equal to 830 V while the power of 30 kW was being transferred to the primary side. Waveforms obtained during this test are given in Fig. 21. Measured efficiency of the system was 95.76%.

From the presented, it is clear that the proposed tuning method and design of the S–S–S compensated three-coil IPT charger satisfies the most important requirements of the current SAE

TABLE VI
COMPARISON WITH OTHER RELEVANT IPT SYSTEMS FROM STATE-OF-THE-ART

Work	Number of coils	Compensation strategy	Application	Bidirectional	Coupling coefficient	Power level	Efficiency
This work	3	Modified S–S–S	EV Charging	Yes	$k_{ps} \in [0.126, 0.258]$ $k_{st} \in [0.140, 0.286]$	3.7 kW–37.4 kW	91.29%–96.72%
[22]	3	S–S–LCLCC	Battery Charging	No	$k_{ps} = 0.02$ $k_{st} \in [0.051, 0.092]$	30 W–840 W	60%–91.2%
[23]	3	S–S–S	EV Charging	No	$k_{ps} \approx 0$ $k_{st} \in [0.071, 0.082]$	60 W–325 W	62.5%–83.5%
[25]	3	Modified S–S–S	General IPT	No	$k_{ps} = 0.191$ k_{st} Unk.	1.1 kW–6.6 kW	94.27%–95.57%
[26]	3	S–S–S and Hybrid Topology	Battery Charging	No	$k_{ps} = 0.023$ $k_{st} = 0.092$	40 W–384 W	50%–90.8%
[29]	3	Hybrid Topology	Battery Charging	No	$k_{ps} \in [0.157, 0.29]$ $k_{st} \in [0.095, 0.24]$	120 W–450 W	80%–92.5%
[30]	3	S–S–P	Battery Charging	No	$k_{ps} = 0.204$ $k_{st} = 0.183$	41 W–258 W	92%–96%
[33]	3	LCC–LCC–S	EV Charging	No	$k_{ps} \in [0, 0.06]$ $k_{st} \in [0.024, 0.078]$	100 W–3.5 kW	32%–90%
[16]	2	LCC–LCC	EV Charging	No	$k_{ps} \in [0.075, 0.175]$	330 W	88.13%–88.3%
[17]	2	LCC–LCC	EV Charging	No	$k_{ps} = 0.3$	0.8 kW–6.6 kW	90.5%–95.1%

standard proposal in terms of the coil sizes and system efficiency, potentially presenting a solution for high-power, high efficiency bidirectional EV charger. The swing in the relative coupling coefficient in this work, that comes as the consequence of considered clearance and misalignment area, is lower then the one predicted by the SAE standard. In this work, we have presented the algorithm how to design the IPT system based on the proposed principles that has, as one of its input parameters, the clearance and misalignment area for which the system is designed. From the analysis presented in this article, it is possible to deduce that with the increase of swing in the relative coupling coefficient, the swing in the system efficiency will increase as well, due to loss of soft-switching conditions. However, the presented system has more than enough margin, in terms of system efficiency and power transfer capability that are defined in the SAE standard, to present a potential candidate for a real-life applications.

VI. CONCLUSION

In the presented work a comprehensive equivalent circuit of the three-coil IPT system is derived. Tuning method for the S–S–S compensated three-coil IPT system, suitable for the high-power and high-efficiency bidirectional EV charger, is proposed. The proposed tuning method leads to the functionality of the system, where seamless implementation both CC/CV and CP/CV charging methodologies is possible, as well as the transition between G2V and V2G modes of operation. Design procedure of the 30 kW IPT system based on the considered three-coil compensation strategy is outlined. Extensive tests with power level ranging between 3.7 kW and 37.4 kW are conducted in order to verify the proposed tuning method, achieving high efficiency, between 91.29% and 96.72%, over the entire range of considered clearances and misalignments, battery voltages, and battery charging currents/power levels, proving the effectiveness and applicability of the proposed tuning method.

REFERENCES

[1] A. Sagar et al., "A comprehensive review of the recent development of wireless power transfer technologies for electric vehicle charging systems," *IEEE Access*, vol. 11, pp. 83703–83751, 2023.

[2] F. Grazian, T. B. Soeiro, and P. Bauer, "Voltage/current doubler converter for an efficient wireless charging of electric vehicles with 400-V and 800-V battery voltages," *IEEE Trans. Ind. Electron.*, vol. 70, no. 8, pp. 7891–7903, Aug. 2023.

[3] O. N. Nezamuddin, C. L. Nicholas, and E. C. d. Santos, "The problem of electric vehicle charging: State-of-the-art and an innovative solution," *IEEE Trans. Intell. Transp. Syst.*, vol. 23, no. 5, pp. 4663–4673, May 2022.

[4] SAE. International, "Wireless power transfer for light-duty plug-in/electric vehicles and alignment methodology," J2954, 10 2022.

[5] W. Zhang and C. C. Mi, "Compensation topologies of high-power wireless power transfer systems," *IEEE Trans. Veh. Technol.*, vol. 65, no. 6, pp. 4768–4778, Jun. 2016.

[6] H. Chen et al., "Modular four-channel 50 kw WPT system with decoupled coil design for fast EV charging," *IEEE Access*, vol. 9, pp. 136083–136093, 2021.

[7] L. Shi, A. Delgado, R. Ramos, and P. Alou, "A wireless power transfer system with inverse coupled current doubler rectifier for high-output current applications," *IEEE Trans. Ind. Electron.*, vol. 69, no. 5, pp. 4607–4616, May 2022.

[8] J. H. Kim et al., "Development of 1-mw inductive power transfer system for a high-speed train," *IEEE Trans. Ind. Electron.*, vol. 62, no. 10, pp. 6242–6250, Oct. 2015.

[9] M. Bertoluzzo, A. Kumar, and A. Sagar, "Control strategy for a bidirectional wireless power transfer system with vehicle to home functionality," *IEEE Access*, vol. 11, pp. 60421–60448, 2023.

[10] K. Chen and Z. Zhang, "Rotating-coordinate-based mutual inductance estimation for drone in-flight wireless charging systems," *IEEE Trans. Power Electron.*, vol. 38, no. 9, pp. 11685–11693, Sep. 2023.

[11] A. Delgado, N. A. Requena, R. Ramos, J. A. Oliver, P. Alou, and J. A. Cobos, "Design of inductive power transfer system with a behavior of voltage source in open-loop considering wide mutual inductance variation," *IEEE Trans. Power Electron.*, vol. 35, no. 11, pp. 11453–11462, Nov. 2020.

[12] C.-S. Wang, O. Stielau, and G. Covic, "Design considerations for a contactless electric vehicle battery charger," *IEEE Trans. Ind. Electron.*, vol. 52, no. 5, pp. 1308–1314, May 2005.

[13] S. Li, W. Li, J. Deng, T. D. Nguyen, and C. C. Mi, "A double-sided LCC compensation network and its tuning method for wireless power transfer," *IEEE Trans. Veh. Technol.*, vol. 64, no. 6, pp. 2261–2273, Jun. 2015.

[14] S. Weerasinghe, U. K. Madawala, and D. J. Thrimawithana, "A matrix converter-based bidirectional contactless grid interface," *IEEE Trans. Power Electron.*, vol. 32, no. 3, pp. 1755–1766, Mar. 2017.

[15] C. S. Wong, J. Liu, L. Cao, and K. H. Loo, "A swiss-rectifier-based single-stage three-phase bidirectional ac–dc inductive-power-transfer converter for vehicle-to-grid applications," *IEEE Trans. Power Electron.*, vol. 38, no. 3, pp. 4152–4166, Mar. 2023.

[16] X. Zhang, R. Xue, F. Wang, F. Xu, T. Chen, and Z. Chen, "Capacitor tuning of LCC-LCC compensated IPT system with constant-power output and large misalignments tolerance for electric vehicles," *IEEE Trans. Power Electron.*, vol. 38, no. 10, pp. 11928–11939, Oct. 2023.

[17] N. Fu, J. Deng, Z. Wang, and D. Chen, "Dual-phase-shift control strategy with switch-controlled capacitor for overall efficiency optimization in wireless power transfer system," *IEEE Trans. Veh. Technol.*, vol. 72, no. 6, pp. 7304–7317, Jun. 2023.

[18] I.-W. Iam, C.-K. Choi, C.-S. Lam, P.-I. Mak, and R. P. Martins, "A constant-power and optimal-transfer-efficiency wireless inductive power transfer converter for battery charger," *IEEE Trans. Ind. Electron.*, vol. 71, no. 1, pp. 450–461, Jan. 2024.

[19] Y. Zhang, R. Liu, H. Wang, X. Mao, and X. Chen, "Current balancing of a multiphase inverter for LCC-S compensated wireless power transfer system based on mutually negatively coupled inductors," *IEEE Trans. Power Electron.*, vol. 38, no. 10, pp. 12411–12415, Oct. 2023.

[20] J. Yang, X. Zhang, K. Zhang, X. Cui, C. Jiao, and X. Yang, "Design of LCC-S compensation topology and optimization of misalignment tolerance for inductive power transfer," *IEEE Access*, vol. 8, pp. 191309–191318, 2020.

[21] W. X. Zhong, C. Zhang, X. Liu, and S. Y. R. Hui, "A methodology for making a three-coil wireless power transfer system more energy efficient than a two-coil counterpart for extended transfer distance," *IEEE Trans. Power Electron.*, vol. 30, no. 2, pp. 933–942, Feb. 2015.

[22] P. Darvish, S. Mekhilef, and H. A. B. Illias, "A novel S–S–LCLCC compensation for three-coil WPT to improve misalignment and energy efficiency stiffness of wireless charging system," *IEEE Trans. Power Electron.*, vol. 36, no. 2, pp. 1341–1355, Feb. 2021.

[23] H. Wang, K. W. E. Cheng, X. Li, and J. Hu, "A special magnetic coupler structure for three-coil wireless power transfer: Analysis, design, and experimental verification," *IEEE Trans. Magn.*, vol. 57, no. 11, pp. 1–8, Nov. 2021.

[24] H. Xu, Z. Huang, Y. Yang, Z. Huang, I.-W. Iam, and C.-S. Lam, "Analysis and design of three-coil coupler for inductive power transfer system with automatic seamless CC-to-CV charging capability," *IEEE Access*, vol. 10, pp. 10139–10148, 2022.

[25] S. Moon, B.-C. Kim, S.-Y. Cho, and G.-W. Moon, "Analysis and design of wireless power transfer system with an intermediate coil for high efficiency," in *Proc. IEEE ECCE Asia Downunder*, 2013, pp. 1034–1040.

[26] Y. Li, Q. Xu, T. Lin, J. Hu, Z. He, and R. Mai, "Analysis and design of load-independent output current or output voltage of a three-coil wireless power transfer system," *IEEE Trans. Transport. Electrific.*, vol. 4, no. 2, pp. 364–375, Feb. 2018.

[27] J. Zhang, X. Yuan, C. Wang, and Y. He, "Comparative analysis of two-coil and three-coil structures for wireless power transfer," *IEEE Trans. Power Electron.*, vol. 32, no. 1, pp. 341–352, Jan. 2017.

[28] Y. Zhang, Z. Shen, W. Pan, H. Wang, Y. Wu, and X. Mao, "Constant current and constant voltage charging of wireless power transfer system based on three-coil structure," *IEEE Trans. Ind. Electron.*, vol. 70, no. 1, pp. 1066–1070, Jan. 2023.

[29] Y. Wang, H. Liu, F. Wu, P. Wheeler, Q. Zhou, and S. Zhao, "Research on a three-coil hybrid IPT charger with improved tolerance to coupling variation and load-independent output," *IEEE J. Emerg. Sel. Topics Ind. Electron.*, vol. 4, no. 2, pp. 625–636, Feb. 2023.

[30] L. Yang, L. Ren, Y. Shi, M. Wang, and Z. Geng, "Analysis and design of an s/s/p-compensated three-coil structure WPT system with constant current and constant voltage output," *IEEE Trans. Emerg. Sel. Topics Power Electron.*, vol. 11, no. 3, pp. 2487–2500, Mar. 2023.

[31] X. Liu, X. Song, and X. Yuan, "Compensation optimization of the relay coil in a strong coupled coaxial three-coil wireless power transfer system," *IEEE Trans. Power Electron.*, vol. 37, no. 4, pp. 4890–4902, Apr. 2022.

[32] D.-W. Seo, "Design method of three-coil WPT system based on critical coupling conditions," *IEEE Trans. Emerg. Sel. Topics Power Electron.*, vol. 9, no. 3, pp. 3802–3811, Mar. 2021.

[33] E. S. Lee, D. Kim, and S. Y. Jeong, "Triangular DQ TX coils of wireless EV chargers for large misalignment tolerances," *IEEE Trans. Veh. Technol.*, vol. 72, no. 11, pp. 14179–14188, Nov. 2023.

[34] A. Bilal, S. Kim, F. Lin, and G. Covic, "Analysis of IPT intermediate coupler system for vehicle charging over large air gaps," *IEEE J. Emerg. Sel. Topics Ind. Electron.*, vol. 3, no. 4, pp. 1149–1158, Apr. 2022.

[35] A. Kamineni, G. A. Covic, and J. T. Boys, "Analysis of coplanar intermediate coil structures in inductive power transfer systems," *IEEE Trans. Power Electron.*, vol. 30, no. 11, pp. 6141–6154, Nov. 2015.

[36] Y. Zhang, Z. Zhao, and T. Lu, "Quantitative analysis of system efficiency and output power of four-coil resonant wireless power transfer," *IEEE Trans. Emerg. Sel. Topics Power Electron.*, vol. 3, no. 1, pp. 184–190, Jan. 2015.

[37] S. Seshadri, M. Kavitha, and P. B. Bobba, "Effect of coil structures on performance of a four-coil WPT powered medical implantable devices," in *Proc. Int. Conf. Power, Instrumentation, Control Comput.*, 2018, pp. 1–6.

[38] C.-L. Yang, C.-K. Chang, S.-Y. Lee, S.-J. Chang, and L.-Y. Chiou, "Efficient four-coil wireless power transfer for deep brain stimulation," *IEEE Trans. Microw. Theory Techn.*, vol. 65, no. 7, pp. 2496–2507, Jul. 2017.

[39] R. Huang and B. Zhang, "Frequency, impedance characteristics and HF converters of two-coil and four-coil wireless power transfer," *IEEE Trans. Emerg. Sel. Topics Power Electron.*, vol. 3, no. 1, pp. 177–183, Jan. 2015.

[40] Y. Zhang, Z. Zhao, and K. Chen, "Frequency-splitting analysis of four-coil resonant wireless power transfer," *IEEE Trans. Ind. Appl.*, vol. 50, no. 4, pp. 2436–2445, Apr. 2014.

[41] S. Moon and G.-W. Moon, "Wireless power transfer system with an asymmetric four-coil resonator for electric vehicle battery chargers," *IEEE Trans. Power Electron.*, vol. 31, no. 10, pp. 6844–6854, Oct. 2016.

[42] M. Kiani, U.-M. Jow, and M. Ghovanloo, "Design and optimization of a 3-coil inductive link for efficient wireless power transmission," *IEEE Trans. Biomed. Circuits Syst.*, vol. 5, no. 6, pp. 579–591, Jun. 2011.

[43] H. T. Nguyen et al., "Review map of comparative designs for wireless high-power transfer systems in EV applications: Maximum efficiency, ZPA, and CC/CV modes at fixed resonance frequency independent from coupling coefficient," *IEEE Trans. Power Electron.*, vol. 37, no. 4, pp. 4857–4876, Apr. 2022.

[44] F. Yang et al., "Misalignment tolerance improvement for loosely coupled transformer of IPT systems via an intermediate coil with detuned compensation," *IEEE Access*, vol. 11, pp. 90181–90189, 2023.

[45] N. Mirkovic, A. Delgado, P. Alou, and M. Vasic, "Increasing power transfer capability of wireless battery charger under misalignment conditions," in *Proc. PCIM Europe Int. Exhib. Conf. Power Electron., Intell. Motion, Renewable Energy Energy Manage.*, 2023, pp. 1–8.

[46] W. Zhong, S. Zhang, M. Chen, and M. D. Xu, "Reconfigurable resonant topology linking two-, three-, and four-coil modes for WPT with large coupling range and fixed frequency," *IEEE Trans. Power Electron.*, vol. 37, no. 7, pp. 8713–8725, Jul. 2022.

[47] F. Xu, S.-C. Wong, and C. K. Tse, "Overall loss compensation and optimization control in single-stage inductive power transfer converter delivering constant power," *IEEE Trans. Power Electron.*, vol. 37, no. 1, pp. 1146–1158, Jan. 2022.

[48] Z. Huang, C.-S. Lam, P.-I. Mak, R. P. d. S. Martins, S.-C. Wong, and C. K. Tse, "A single-stage inductive-power-transfer converter for constant-power and maximum-efficiency battery charging," *IEEE Trans. Power Electron.*, vol. 35, no. 9, pp. 8973–8984, Sep. 2020.

[49] L.-R. Chen, J.-J. Chen, N.-Y. Chu, and G.-Y. Han, "Current-pumped battery charger," *IEEE Trans. Ind. Electron.*, vol. 55, no. 6, pp. 2482–2488, Jun. 2008.

[50] L. Jiang et al., "Optimal charging strategy with complementary pulse current control of lithium-ion battery for electric vehicles," *IEEE Trans. Transport. Electrific.*, vol. 8, no. 1, pp. 62–71, Jan. 2022.

[51] N. Mirković, D. Stojić, A. Delgado, P. Alou, and M. Vasić, "Novel three phase to single phase matrix converter modulation strategy for bidirectional inductive power transfer," *IEEE Trans. Power Electron.*, vol. 38, no. 12, pp. 14830–14846, Dec. 2023.

[52] B. Zhao, Q. Song, W. Liu, and Y. Sun, "Overview of dual-active-bridge isolated bidirectional dc–dc converter for high-frequency-link power-conversion system," *IEEE Trans. Power Electron.*, vol. 29, no. 8, pp. 4091–4106, Aug. 2014.

[53] F. Liu, K. Li, K. Chen, and Z. Zhao, "A phase synchronization technique based on perturbation and observation for bidirectional wireless power transfer system," *IEEE Trans. Emerg. Sel. Topics Power Electron.*, vol. 8, no. 2, pp. 1287–1297, Feb. 2020.

[54] T. Tan, K. Chen, Y. Jiang, Q. Lin, L. Yuan, and Z. Zhao, "A bidirectional wireless power transfer system control strategy independent of real-time wireless communication," *IEEE Trans. Ind. Appl.*, vol. 56, no. 2, pp. 1587–1598, Feb. 2020.

[55] M. T. Lawder et al., "Battery energy storage system (BESS) and battery management system (BMS) for grid-scale applications," *Proc. IEEE*, vol. 102, no. 6, pp. 1014–1030, Jun. 2014.

[56] A. Delgado, D. Schoenberger, J. Á. Oliver, P. Alou, and J. A. Cobos, "Design guidelines of inductive coils using a polymer bonded magnetic composite for inductive power transfer systems in electric vehicles," *IEEE Trans. Power Electron.*, vol. 35, no. 8, pp. 7884–7893, Aug. 2020.
[57] A. D. Expósito, "Analysis and guidelines for inductive power transfer link design," Ph.D. dissertation, Universidad Politécnicade Madrid, E.T.S.I.I., 2021.
[58] A. Delgado, G. Salinas, J. A. Oliver, J. A. Cobos, and J. Rodriguez-Moreno, "Equivalent conductor layer for fast 3-D finite element simulations of inductive power transfer coils," *IEEE Trans. Power Electron.*, vol. 35, no. 6, pp. 6221–6230, Jun. 2020.

Nikola Mirković (Student Member, IEEE) was born in Belgrade, Serbia, in 1997. He received the B.Sc. and M.Sc. degrees in electrical engineering from the Faculty of Electrical Engineering, University of Belgrade, Belgrade, Serbia, in 2020 and 2021, respectively. He is currently working toward the Ph.D. degree in industrial electronics from Centro de Electrónica Industrial, Universidad Politécnica de Madrid, Madrid, Spain.

Since 2021. he is a Member of Centro de Electrónica Industrial, Universidad Politécnica de Madrid (UPM). His research interests comprise inductive power transfer and power converters.

Luis Ruiz Chamorro was born in Madrid, Spain, in 1999. He received the M.Sc. degree in industrial engineering from the Universidad Politécnica de Madrid, Madrid, Spain, in 2023.

He is currently working as a Researcher with Centro de Electrónica Industrial (CEI-UPM).

Alberto Delgado (Member, IEEE) received the B.Sc. degree in electrical engineering from the University of Malaga, Malaga, Spain, in 2016, and the M.Sc. and Ph.D. degrees in industrial electronics from the Polytechnic University of Madrid (UPM), Madrid, Spain, in 2017 and 2021, respectively.

He became a Teaching Assistant with UPM, in 2019. His research interests include modeling of dc–dc converters for inductive power transfer systems and magnetic components for different applications, such as RFID communications and wireless charging and magnetic nano-materials and micro-materials.

Dr. Delgado was awarded honours on several occasions, during his undergraduate studies and he achieved the Best Student of the Year Award.

Pedro Alou (Member, IEEE) was born in Madrid, Spain, in 1970. He received the M.S. and Ph.D. degrees in electrical engineering from the Universidad Politécnica de Madrid (UPM), Madrid, Spain, in 1995 and 2004, respectively.

Currently, he is Full Professor with UPM. He has been involved in Power Electronics since 1995, participating in more than 70 R&D projects with the industry. He has authored or coauthored more than 45 journal articles, 140 conference papers and holds six patents. His research interests include power converters, advanced topologies for efficient energy conversion, modeling of converters and magnetic components, advanced control techniques for high dynamic response, energy management and new semiconductor technologies for power electronics. His research activity is distributed among industrial, aerospace, and military projects.

Miroslav Vasić (Senior Member, IEEE) was born in Serbia in 1981. He received the B.S. degree in electrical engineering from the School of Electrical Engineering, University of Belgrade, Belgrade, Serbia, in 2005. He received the M.S. and Ph.D. degrees in industrial electronics both from Centro de Electrónica Industrial at ETSII (UPM), in 2007 and 2010.

Since then, he has been working with Centro de Electrónica Industrial at ETSII (UPM). He has been working as an Associate Professor with UPM since 2019. In the recent years great part of his research activities has been related to the research of new semiconductor devices based on GaN and their impact on power electronics. His research interest includes application of power converters and their optimization.

Miroslav Vasić has authored or coauthored more than 70 peer-reviewed technical papers at conferences and in IEEE journals and he advised five Ph.D. thesis and holds six patents. He actively serves as an Associated Editor with IEEE JOURNAL OF EMERGING AND SELECTED TOPICS IN POWER ELECTRONICS AND IEEE TRANSACTIONS ON VEHICULAR TECHNOLOGY. He was one of the co-founders of the IEEE PELS TC 10- Design Methodologies and acted as the Vice-chair from 2021 until 2023. In 2012, he was a recipient of the Semikron Innovation Award for the teamwork on RF Power Amplifier with Increased Efficiency and Bandwidth. In 2015, he received a medal from Spanish Royal Academy of Engineering as a recognition of his research trajectory and in 2016, he received UPM Research Projection Award for the best young Researcher with Universidad Politécnica de Madrid.